




Assimilatory sulfate reduction in the marine methanogen *Methanothermococcus thermolithotrophicus*

Received: 28 February 2023

Marion Jespersen  & Tristan Wagner  

Accepted: 26 April 2023

Published online: 5 June 2023

 Check for updates

Methanothermococcus thermolithotrophicus is the only known methanogen that grows on sulfate as its sole sulfur source, uniquely uniting methanogenesis and sulfate reduction. Here we use physiological, biochemical and structural analyses to provide a snapshot of the complete sulfate reduction pathway of this methanogenic archaeon. We find that later steps in this pathway are catalysed by atypical enzymes. PAPS (3'-phosphoadenosine 5'-phosphosulfate) released by APS kinase is converted into sulfite and 3'-phosphoadenosine 5'-phosphate (PAP) by a PAPS reductase that is similar to the APS reductases of dissimilatory sulfate reduction. A non-canonical PAP phosphatase then hydrolyses PAP. Finally, the F₄₂₀-dependent sulfite reductase converts sulfite to sulfide for cellular assimilation. While metagenomic and metatranscriptomic studies suggest that the sulfate reduction pathway is present in several methanogens, the sulfate assimilation pathway in *M. thermolithotrophicus* is distinct. We propose that this pathway was 'mix-and-matched' through the acquisition of assimilatory and dissimilatory enzymes from other microorganisms and then repurposed to fill a unique metabolic role.

The most common methane-producing microorganisms have a high demand for sulfur due to their specific enzymes and metabolism. While most of these methanogens use sulfides (HS⁻), some have been shown to metabolize higher oxidation states of sulfur or even metal sulfides (for example, FeS₂) for sulfur acquisition^{1–5}. However, *Methanothermococcus thermolithotrophicus* is the only known methanogen capable of growing on sulfate (SO₄²⁻) as its sole sulfur source^{4,6}. The metabolism of this marine hydrogenotroph, isolated from geothermally heated sea sediments near Naples (Italy), is paradoxical, as SO₄²⁻ reduction should lead to several physiological obstacles for a methane-producing microbe. First, methanogens commonly thrive in reduced sulfidic environments where all electron acceptors other than CO₂ are depleted, including SO₄²⁻ (refs. 7,8). Second, at the interface where methanogens and SO₄²⁻ ions coexist, hydrogenotrophic methanogens must compete with dissimilatory SO₄²⁻-reducing microorganisms for the common substrate dihydrogen (H₂)⁹. Third, methanogens live at the thermodynamic limits of life and the adenosine

triphosphate (ATP) hydrolysis coupled to SO₄²⁻ reduction would be a substantial investment for such energy-limited microorganisms^{8,10}. Finally, the SO₄²⁻ reduction pathway generates toxic intermediates that would interfere with cellular processes.

To assimilate SO₄²⁻, the organism would have to capture the anion and transport it into the cell using a transporter. Inside the cell, SO₄²⁻ is activated by an ATP sulfurylase (ATPS) to generate adenosine 5'-phosphosulfate (APS)^{11–13}. From there, organisms can use different strategies (Extended Data Fig. 1, routes a–c): (1a) APS is directly reduced by an APS reductase (APSR) to generate AMP and SO₃²⁻. (1b) Alternatively, APS can be further phosphorylated to 3'-phosphoadenosine 5'-phosphosulfate (PAPS) by the APS kinase (APSK). A PAPS reductase (PAPSR) will reduce PAPS to SO₃²⁻ and the toxic nucleotide 3'-phosphoadenosine 5'-phosphate (PAP). PAP must be quickly hydrolysed to AMP and inorganic phosphate by a PAP phosphatase (PAPP). In both scenarios, the final step is carried out by a siroheme-containing sulfite reductase, which reduces the SO₃²⁻ into HS⁻. The latter can then

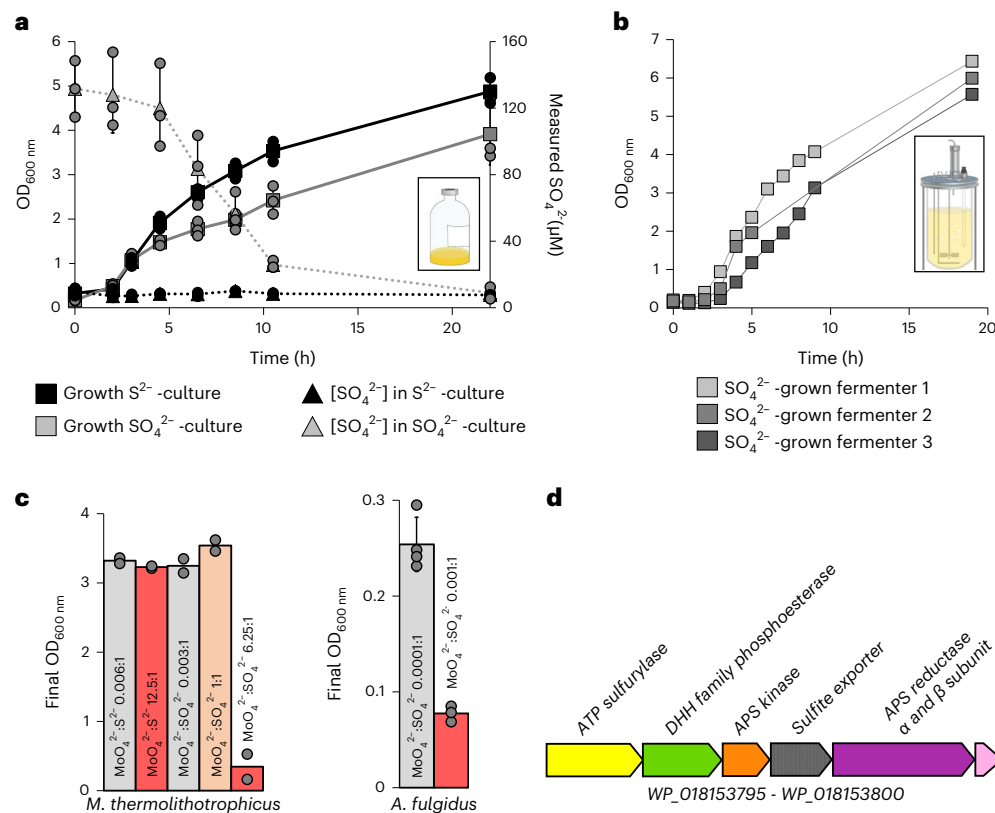


Fig. 1 SO₄²⁻ growth dependency of *M. thermolithotrophicus*.

a, *M. thermolithotrophicus* cultures grown on Na₂S (black squares, 0.5 mM) and Na₂SO₄ (grey squares, 0.5 mM). The consumption or release of SO₄²⁻ in Na₂S or Na₂SO₄ cultures are shown by black and grey triangles, respectively. Data are presented as mean ± s.d. and individual values are shown as spheres ($n = 3$ replicates). Differences between expected (0.5 mM) and measured (0.13 mM) SO₄²⁻ concentration for the initial point are considered to be due to an artefact from the medium (see Methods). **b**, *M. thermolithotrophicus* grown on 10 mM

Na₂SO₄ in three independent fermenters. The sampling points are represented by grey squares. **c**, Molybdate (Na₂MoO₄) inhibition of Na₂SO₄ assimilatory and dissimilatory archaea. Growth experiments for *M. thermolithotrophicus* were performed in duplicates and for *A. fulgidus* in quadruplicates (left) or triplicates (right). Data are represented as mean and for the triplicates and quadruplicates ± s.d. **d**, Predicted operon for SO₄²⁻ reduction from the whole-genome shotgun sequence of *M. thermolithotrophicus*.

be incorporated into biomass. (1c) In a different pathway, the sulfite group of PAPS is transferred to another acceptor to build up sulfated metabolites. Route 1a is very similar to the dissimilatory pathway (Extended Data Fig. 1, route 2). However, dissimilatory APSRs and dissimilatory sulfite reductases are structurally and phylogenetically distinct from their assimilatory counterparts and indirectly couple their reactions to membrane pumps, allowing for energy conservation^{14–16}.

Genes encoding putative enzymes associated with SO₄²⁻ reduction have been found in the genomes of multiple methanogens¹³, including *M. thermolithotrophicus*. For this methanogen, a theoretical, albeit incomplete, SO₄²⁻ assimilation pathway can be hypothesized. Here we elucidated the complete SO₄²⁻ reduction machinery of this archaeon and describe how this one methanogen can convert SO₄²⁻ into an elementary block of life.

Results

A marine methanogen consuming SO₄²⁻

Cultures grown on Na₂S were successively transferred to a sulfur-free medium until no growth was observed. *M. thermolithotrophicus* showed robust growth when at least 100 μM of Na₂SO₄ was supplemented in the medium and reached similar cell yields as the Na₂S-grown culture. Under these cultivation conditions, SO₄²⁻ is consumed over time as cell density increases (Fig. 1a). When cells are grown only on Na₂S, no SO₄²⁻ could be detected (Fig. 1a), indicating that *M. thermolithotrophicus* is not performing sulfide oxidation.

We then challenged the SO₄²⁻-grown culture by switching from batch to fermenter conditions, where H₂S can escape to the gas phase and does not accumulate compared to flask conditions. In this open system with temperature and pH controlled, *M. thermolithotrophicus* grew to a maximum optical density (OD)_{600nm} of 6.45 within 19 h (Fig. 1b).

One way to determine whether *M. thermolithotrophicus* relies on canonical enzymes of the SO₄²⁻ reduction pathway is to use molybdate (MoO₄²⁻). The structural analogue of SO₄²⁻ binds to the ATPs and triggers molybdolysis, which hydrolyses ATP to AMP and pyrophosphate (PP_i), resulting in cellular energy depletion^{17,18}. A MoO₄²⁻:SO₄²⁻ molar ratio of 0.004:1 is sufficient to inhibit the activity of dissimilatory SO₄²⁻-reducing bacteria for 168 h, an effect mainly due to molybdolysis by ATPs^{19–21}. SO₄²⁻ assimilation is also affected by MoO₄²⁻, as demonstrated by studies on plants²². In the latter, growth inhibition occurred when MoO₄²⁻ was in excess compared to SO₄²⁻ and the ATPs activity was notably affected at a 1:1 ratio¹⁸. When applied on *M. thermolithotrophicus*, a high MoO₄²⁻:Na₂S ratio of 12.5:1 did not disturb growth of the Na₂S culture, indicating that MoO₄²⁻ is not interfering with their basal metabolism. In contrast, a MoO₄²⁻:SO₄²⁻ ratio of 6.25:1 was inhibitory to the SO₄²⁻-grown culture, while a 1:1 ratio was not (Fig. 1c and Extended Data Fig. 2a). SO₄²⁻ addition to the MoO₄²⁻-inhibited culture restored growth (Extended Data Fig. 2b), indicating the reversibility of inhibition and its strict control by the MoO₄²⁻:SO₄²⁻ ratio rather than the MoO₄²⁻ concentration. In comparison, in *Archaeoglobus fulgidus*, an archaeon that performs dissimilatory SO₄²⁻ reduction to conserve energy, we observed growth inhibition at a MoO₄²⁻:SO₄²⁻ ratio of 0.001:1 (Fig. 1c

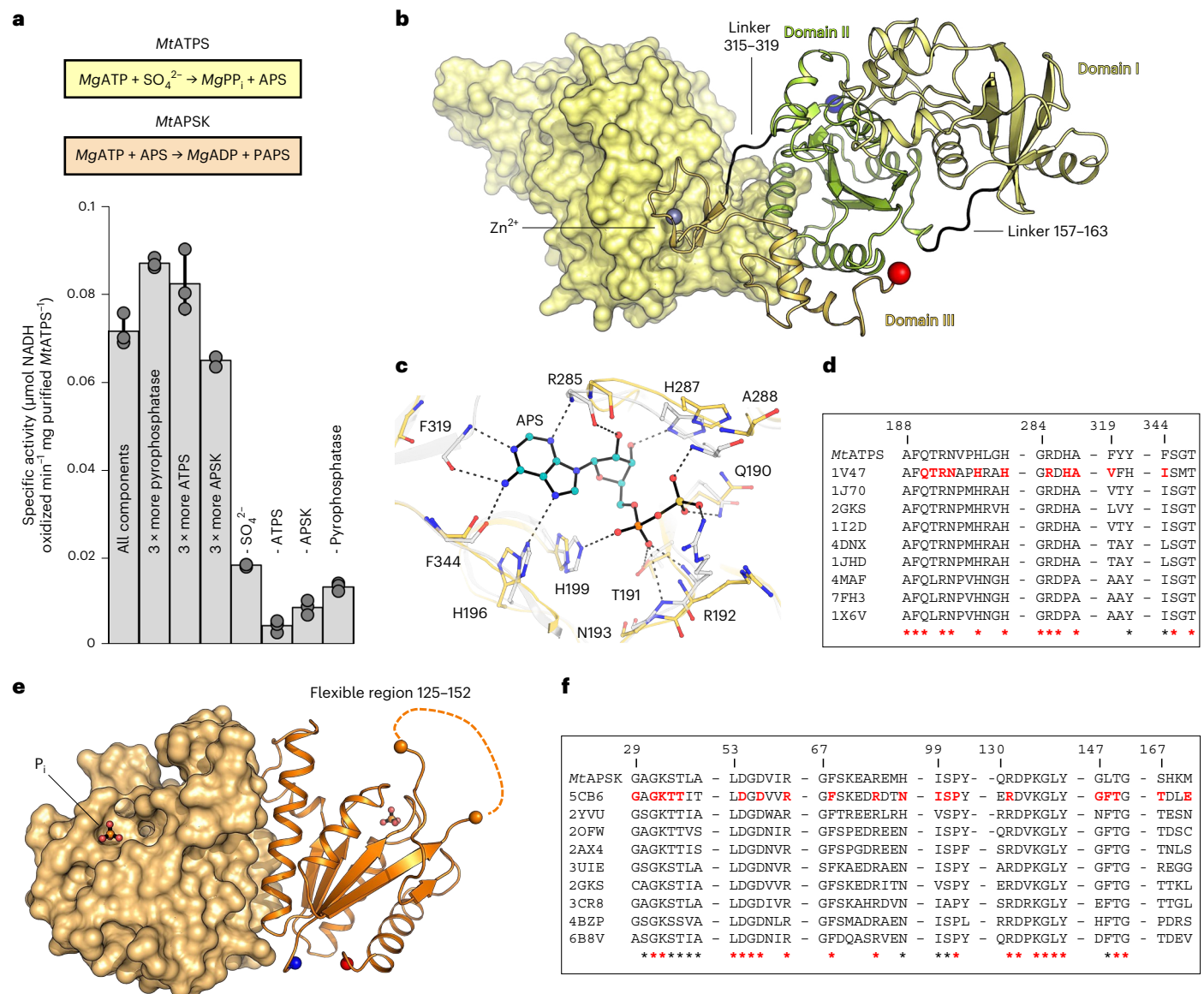


Fig. 2 | *MtATPS* and *MtAPSK* catalyse the first steps of the SO_4^{2-} reduction pathway. **a**, Top panel, reactions catalyzed by *MtATPS* and *MtAPSK*; Bottom panel, the specific activity of *MtATPS* and *MtAPSK*, determined via a coupled enzyme assay. ‘-’ indicates the absence of the indicated reactant. Data are presented as mean \pm s.d. and individual values are shown as grey spheres ($n = 3$ replicates). **b**, *MtATPS* homodimeric structure in which one monomer is shown in light yellow surface and the other one in cartoon. **c**, Active site of *MtATPS* (yellow) superposed on the ATPS from *Thermus thermophilus* HB8 (PDB: 1V47, grey) containing the APS shown as balls and sticks with carbons coloured cyan. Residues involved in substrate binding are highlighted in sticks and only the ones

from *MtATPS* are labelled. Hydrogen bonds between the ATPS from *T. thermophilus* and APS are represented as dashed lines. Nitrogen, oxygen, phosphorus and sulfur are coloured in blue, red, orange and yellow, respectively. **d**, Sequence conservation across ATPS homologues. **e**, *MtAPSK* homodimeric structure in which one monomer is shown in light orange surface and the other one in cartoon. The flexible loop illustrated by the dashed line could not be modelled. In all structures, the N and C termini are shown by a blue and red sphere, respectively. **f**, Sequence conservation across APSK homologues. For **d** and **f**, red bold residues are involved in substrate binding, while red and black stars are perfectly and well-conserved residues, respectively.

and Extended Data Fig. 2c). These results suggest that *M. thermolithotrophicus* reduces SO_4^{2-} via an assimilatory pathway containing a functional ATPS. Genes coding for putative standalone ATPS and APSK were indeed on the same locus in the genome of the strain DSM2095 that we had re-sequenced (Fig. 1d) (refs. 13,23). To confirm their functions, the ATPS and APSK from *M. thermolithotrophicus* (*MtATPS* and *MtAPSK*, respectively) were further characterized.

A classic ATPS/APSK to activate SO_4^{2-}

The activity of the recombinantly expressed *MtATPS* and *MtAPSK* was tested via a coupled assay (Fig. 2a and Supplementary Fig. 1) and a

specific activity of $0.070 \pm 0.004 \mu\text{mol of oxidized NADH min}^{-1} \text{mg}^{-1}$ of *MtATPS* was measured. Under these conditions, the rate-limiting step was the pyrophosphatase activity. This highlights the need for rapid pyrophosphate degradation (Fig. 2a) to avoid a retro-inhibition as previously shown for other ATPS²⁴. A $MoO_4^{2-}:SO_4^{2-}$ ratio of 1:1.25 decreased the activity by half (see Methods), corroborating that ATPS is also reacting with MoO_4^{2-} as shown in other homologues^{8,21}.

The structure of *MtATPS* was refined to 1.97 Å resolution and obtained in an apo state despite co-crystallization with APS and SO_4^{2-} (Extended Data Table 1). While the crystal packing suggests a homotrimeric assembly in two crystalline forms, size exclusion

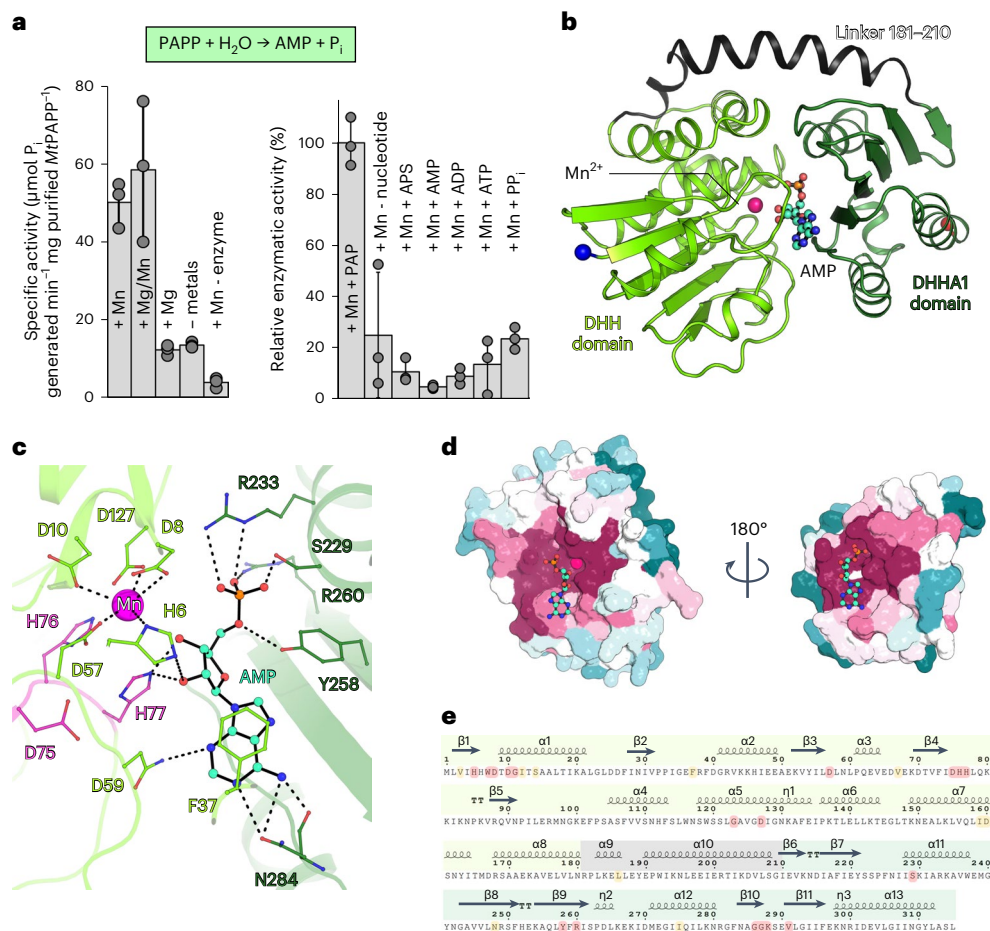


Fig. 3 | A unique type of PAP phosphatase. **a**, Top panel, reaction catalysed by *MtPAPP*; Bottom panel, specific activity of the *MtPAPP* determined via the production of P_i (left) and relative enzymatic activity towards different nucleotides (right). Data are presented as mean \pm s.d. and individual values are shown as grey spheres ($n = 3$ replicates). **b**, Organization of *MtPAPP* shown in cartoon representation. The N and C termini are highlighted as blue and red balls, respectively. Carbon, nitrogen, oxygen and phosphorus of AMP is coloured as cyan, blue, red and orange, respectively. **c**, Close-up view of the active site of *MtPAPP*. The residues coordinating the AMP and Mn^{2+} ion are highlighted by sticks and coloured as in **b**, with the residues from the DHH motif coloured in

pink. **d**, Cut-through view of *MtPAPP* structure shown in surface representation and coloured by its sequence conservation across 168 archaeal homologues. The colour gradient ranges from variable (teal) to conserved (magenta). **e**, Secondary structure representation was done with ESPrnt 3.0 (ref. 61). The coloured frame corresponds to the different domains: DHH domain in light green, linker in grey and DHHA1 domain in darker green. Perfectly and well-conserved residues across 168 archaeal homologues are highlighted in red and yellow, respectively. The secondary structures composing *MtPAPP* are labelled, in which β -sheets, α -helices, and β -turns are highlighted as arrows, springs and bold TT, respectively.

chromatography and surface analysis using PISA (www.ebi.ac.uk/pdb/e/pisa/) confirmed a homodimeric state similar to bacterial homologues (Extended Data Fig. 3a and Supplementary Fig. 2). The structure exhibits the typical ATPS fold comprising three domains (domain I, 1–156; domain II, 164–314 and domain III, 320–382; Fig. 2b). The dimeric interface is mainly organized by domain III as observed in *T. thermophilus*, a notable difference compared with other structural homologues (Extended Data Fig. 3a,b) (refs. 25–27). Similar to many thermophilic bacteria and archaea, the domain III contains a zinc-binding domain (320–343; Extended Data Fig. 3c,d) that might contribute to thermal stability²⁷. *MtATPS* superposition with structural homologues shows a slight domain rearrangement probably due to the absence of substrate (Extended Data Fig. 3b). All residues critical for the reaction are conserved in *MtATPS*, arguing for a conserved reaction mechanism (Fig. 2c,d, Extended Data Figs. 3e,f and 4a, and Supplementary Fig. 3).

The APS-kinase model from *M. thermolithotrophicus*, *MtAPSK*, was refined to 1.77 Å. *MtAPSK* forms a homodimer with an organization very similar to bacterial enzymes, which was expected due to its high sequence conservation (Extended Data Figs. 4b and 5a).

Despite co-crystallization and soaking the crystals with APS and MgCl_2 , the *MtAPSK* structure was obtained in its apo state with a bound phosphate at the expected position of the ATP β -phosphate (Fig. 2e and Extended Data Fig. 5b,c). The N terminus and region 125–152 (the latter being involved in substrate binding^{28,29}) could not be modelled due to the lack of electron density. However, the residues binding the substrates and Mg^{2+} are conserved (Fig. 2f, Extended Data Fig. 5b,c and Supplementary Fig. 4), suggesting that *MtAPSK* should be functional, as confirmed by the coupled enzyme assay.

An exonuclease-derived PAP phosphatase

If the ATPS and APSK are active, they will produce PAPS, an intermediate that could follow the metabolic routes 1b or 1c (Extended Data Fig. 1). Both routes will lead to the production of the toxic product PAP, which inhibits sulfotransferases and exoribonucleases, and disrupts RNA catabolism^{30,31}. Therefore, it needs to be efficiently hydrolysed by a PAP phosphatase. While the genome did not contain any related PAP phosphatase, a gene coding for a putative phosphoesterase (Fig. 1d) was found in the genomic environment harbouring the ATPS and APSK genes. This PAP-phosphatase candidate, belonging to the

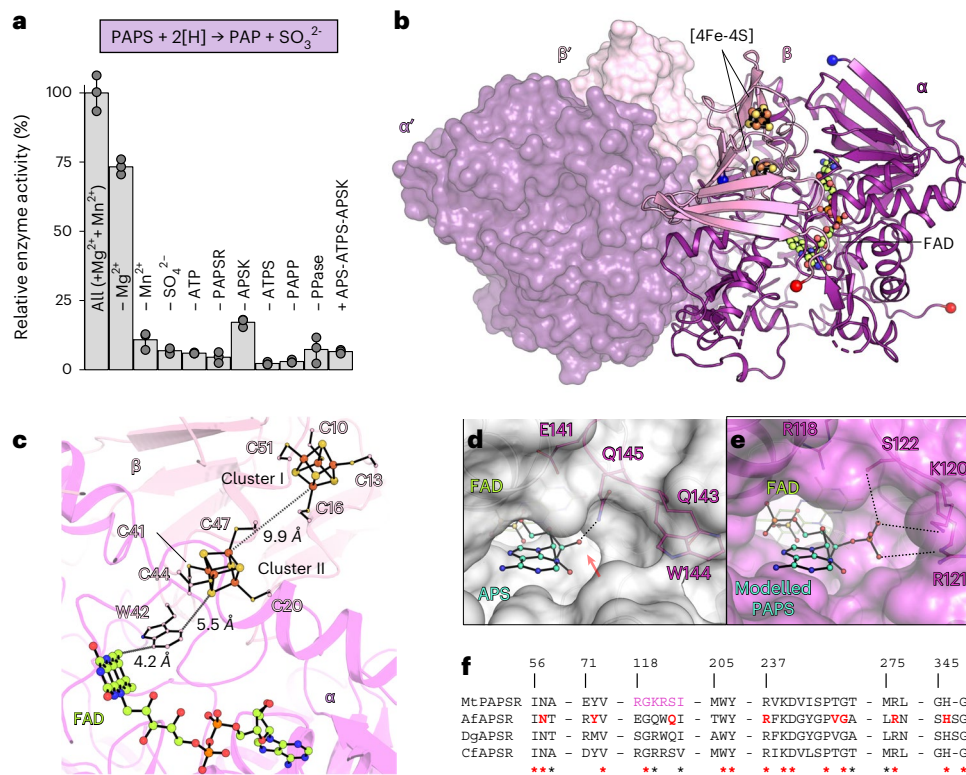


Fig. 4 | *MtPAPSR* has a dissimilatory APS-reductase architecture but is specific to PAPS. **a**, Top panel, reaction catalyzed by *MtPAPSR*; Bottom panel, relative enzyme activity of *MtPAPSR*, determined via a coupled enzyme assay (Extended Data Fig. 8). Data are presented as mean \pm s.d. and individual values are shown as grey spheres ($n = 3$ replicates). **b**, *MtPAPSR* organization with one heterodimer in surface representation and the other in cartoon. N and C termini of both subunits are shown as balls and coloured in blue and red, respectively. Heterodimeric partners are labelled with a prime. Carbon, nitrogen, oxygen, phosphorus, iron and sulfur are coloured in lemon, blue, red, orange, brown and yellow, respectively. **c**, Close-up of cofactors and the electron flow. [4Fe-4S] clusters and cysteines coordinating them, FAD and the Trp42 proposed to participate in the electron transfer are shown in sticks and balls and coloured

as in **b, d, e**. Active sites of APSR (**d**) from *A. fulgidus* containing APS (*AfAPSR*, PDB: 2FJA) and *MtPAPSR* with an artificially modelled PAPS (**e**) shown with a transparent surface. Residues involved in substrate recognition (based on modelled PAPS) are in balls and sticks and coloured as in **b**. A red arrow points to where PAPS would clash. **f**, Sequence conservation across the alpha subunit of *MtPAPSR*, *AfAPSR*, *Megalodesulfovibrio gigas* (*DgAPSR*, PDB: 3GYX) and the putative APSR from *Caldanaerobius fijiensis* (*CfAPSR*, WP_073344903), which shares 68% sequence identity with *MtPAPSR*. Residues involved in APS binding for APSR are in bold and red; perfectly and well-conserved residues are highlighted with red and black stars, respectively. Trp206 and Tyr207 are involved in FAD binding. The sequence alignment was done with MUSCLE⁶².

DHH family, was recombinantly expressed and produced inorganic phosphate (P_i) from PAP at fast rates ($50.2 \pm 5.9 \mu\text{mol of P}_i \text{ released min}^{-1} \text{mg}^{-1}$ of purified enzyme with manganese). The activity was stimulated by manganese addition and showed a high specificity towards PAP (Fig. 3a).

To decipher the mechanism of this uncanonical PAP phosphatase (named *MtPAPP*), the enzyme was co-crystallized with manganese and PAP. The structure, solved by molecular replacement with a template generated by AlphaFold2 (refs. 32,33), was refined to 3.1 Å resolution and contained the product AMP and an ion in its active site, modelled as a partially occupied Mn²⁺ (Extended Data Table 1). While the *MtPAPP* sequence does not align with homologues belonging to the DHH family (except for the DHH motif), it shares an overall fold similar to the exonuclease RecJ or the oligoribonuclease NrnA from *Bacillus subtilis* (*BsNrnA*, which also exhibits PAP-phosphatase activity; Extended Data Fig. 6a) (refs. 34–36). The monomer is composed of an N-terminal (DHH, residues 1–180) and a C-terminal domain (DHHA1, residues 211–315) interconnected by a linker region (residues 181–210), forming a central groove (Fig. 3b). The DHH domain contains the catalytic site and the DHHA1 domain serves as a scaffold to bind the substrate with high specificity (Fig. 3b,c and Extended Data Fig. 6b). The motif coordinating the Mn²⁺ ion in RecJ and *BsNrnA* is perfectly conserved in *MtPAPP*^{34,36}, therefore we expect that in its active state, *MtPAPP* would

be loaded with two Mn²⁺. The first one, partially observed in the structure, is coordinated by four aspartates (Asp8, Asp10, Asp57, Asp127) and a long-range interaction with His6. The absent second Mn²⁺ would be coordinated by the Asp10, Asp57, Asp127, the DHH motif (His76, His77) as well as by water molecules (Extended Data Fig. 6c). While the AMP shares a similar localization with structural homologues ($\beta 9\beta 10\beta 11$), it is bound by a different interaction with the protein (Extended Data Fig. 6b and Supplementary Fig. 5). The nucleotide binding site would ideally place the 3'-phosphate of the PAP in front of the manganese when the enzyme is in its closed state (Extended Data Fig. 6c). The inter-domain movement, allowed by the linker, would facilitate a rapid exchange of the substrate/product, increasing the turnover of *MtPAPP*. The complete sequence of this PAP phosphatase was found in the genome of 168 archaea in which the nucleotide binding site is conserved (Fig. 3d,e and Supplementary Fig. 6). This suggests a common enzyme in archaea to detoxify PAP (Extended Data Fig. 7a).

A dissimilatory APSR-like enzyme reduces PAPS

No genes encoding for a canonical PAPS reductase (route 1b) or sulfo-transferase (route 1c) were found in the *M. thermolithotrophicus* genome. However, genes annotated as dissimilatory APS reductase (α and β subunit, APSR; Extended Data Fig. 7b and Supplementary Fig. 7) are present and co-occur with the previously described genes (Fig. 1d).

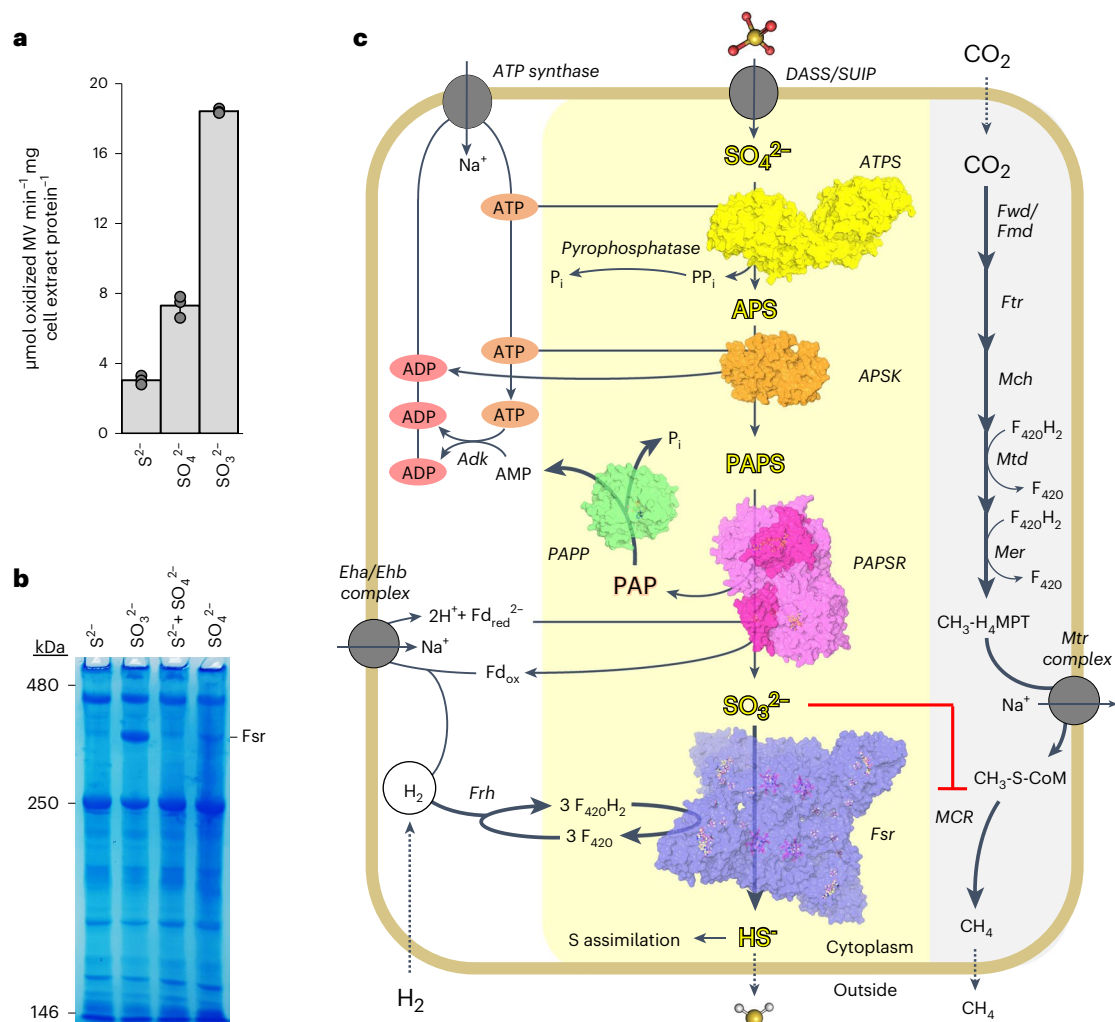


Fig. 5 | Proposed SO₄²⁻ assimilation pathway in a methanogen. a, Sulfite-reductase activity in cell extract from *M. thermolithotrophicus* grown on different sulfur sources. Data are presented as mean ± s.d. and individual values are shown as grey spheres ($n = 3$ biologically independent replicates). **b**, hrCN gel with *M. thermolithotrophicus* cell extract grown on different sulfur sources (15 μg protein loaded per sample, $n = 2$ biologically independent duplicates). **c**, Proposed SO₄²⁻ assimilation pathway in *M. thermolithotrophicus*. Yellow and grey backgrounds highlight the SO₄²⁻ reduction and methanogenesis pathways, respectively. Thick arrows indicate high metabolic fluxes. The structures of the enzymes operating the SO₄²⁻ assimilation pathway are shown in surface representation, with ligands

as balls and sticks. Enzymes are abbreviated as follows: Fwd/Fmd, formylmethanofuran dehydrogenases; Ftr, tetrahydromethanopterin (H₄MPT) formyltransferase; Mch, methenyl-H₄MPT cyclohydrolase; Mtd, methylene-H₄MPT dehydrogenase; Mer, 5,10-methylene-H₄MPT reductase; Mtr, N⁵-CH₃-H₄MPT: coenzyme M methyl-transferase; Mcr, methyl-coenzyme M reductase; Adk, adenylate kinase; Frh, F₄₂₀-reducing [NiFe]-hydrogenase; Eha/Ehb, energy-converting hydrogenase. The putative SO₄²⁻ transporters belonging to the class DASS/SUIP are proposed to be WP_018154444/WP_018154062 and the pyrophosphatase WP_018154121.

To experimentally confirm the activity and substrate specificity of this APS-reductase-like enzyme, both subunits were co-expressed in *Escherichia coli*, purified and tested for enzyme activity assays (Fig. 4a). In contrast to dissimilatory APSRs which catalyse the reversible reduction of APS to AMP and SO₃²⁻ (refs. 37,38), we could not measure the reverse reaction (that is, AMP and SO₃²⁻, or PAP and SO₃²⁻ as substrates) for *M. thermolithotrophicus* enzyme by using K₃Fe(CN)₆ as an electron acceptor. Instead, we used a coupled enzyme assay to reconstitute the pathway in vitro (Extended Data Fig. 8). *Mt*ATPS, a pyrophosphatase and the *Mt*APSK were used to generate PAPS and *Mt*PAPP was added to remove PAP, a potential retro-inhibitor of the reaction³⁹. The activity was monitored via the oxidation of reduced methyl viologen (MV_{red}). When all components were present, a specific enzymatic activity of 0.114 ± 0.007 μmol of oxidized MV min⁻¹ mg⁻¹ of the APS-reductase-like enzyme was measured. A fivefold excess of the APS-reductase-like enzyme resulted in a 220% increase of the specific enzyme activity, indicating that the enzyme was the rate-limiting step

of the reaction (Extended Data Fig. 8c). However, the accumulation of PAP (induced by the removal of *Mt*PAPP or Mn²⁺) strongly inhibited the activity. The specific enzymatic activity with APS as a substrate (that is, removal of *Mt*APSK) was 0.007 ± 0.001 μmol of oxidized MV min⁻¹ mg⁻¹ of the APS-reductase-like enzyme (Fig. 4a). Considering the complexity of this coupled enzyme assay, kinetic parameters could not be determined. However, the assay did provide insights about the substrate specificity and confirmed that the APS-reductase-like enzyme from *M. thermolithotrophicus* exhibits traits of a PAPS reductase.

To gain further molecular insights into the unconventional APS-reductase-like enzyme from *M. thermolithotrophicus*, the enzyme was crystallized under anaerobic conditions. The structure was solved by a single-wavelength anomalous dispersion experiment measured at the Fe K-edge and refined to 1.45 Å resolution (Extended Data Table 1). The complex organizes as an α2β2 heterotetramer, with the same assembly as dissimilatory APS reductases (Fig. 4b and Extended

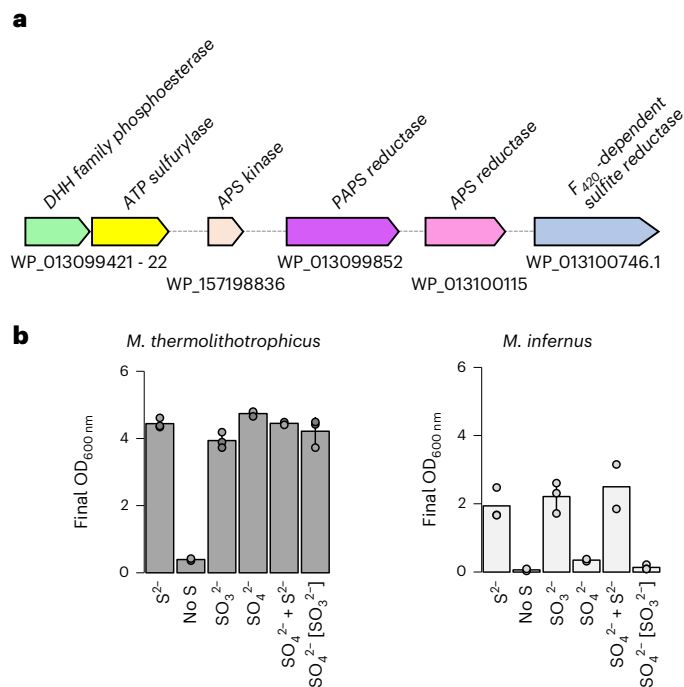


Fig. 6 | SO₄²⁻ reduction potential in Methanococcales. a, *Methanocaldococcus infernus* has the genomic potential to perform the whole SO₄²⁻ assimilation pathway. WP_013099421 has 59.68% amino acid sequence identity with the MtPAPP, WP_013099422 has 70.60% sequence identity with MtATPS and WP_157198836 has 75.44% sequence identity with MtAPSK. The APSR (WP_013100115) and PAPS (WP_013099852) are similar to the biochemically characterized APSR and PAPS from *M. jannaschii* (68.64% and 58.35% amino acid sequence identity, respectively), which have been shown to reduce APS/PAPS^{44,45}. WP_013099852 is not homologous to MtPAPS but homologous to WP_018154242, a putative PAPS reductase in *M. thermolithotrophicus*. WP_013100746 has 65.30% sequence identity to Group I MtFsr. **b**, Growth of *M. thermolithotrophicus* and *M. infernus* on 2 mM Na₂S, without an additional sulfur source, 2 mM Na₂SO₃, 2 mM Na₂SO₄ or 2 mM Na₂SO₄ with 2 mM Na₂S. The SO₃²⁻ in brackets indicates that it was used as the sulfur substrate for the inoculum. Represented are the maximum OD_{600nm} of the cultures, in triplicates, shown as mean ± s.d. *M. infernus* cultures grown without sulfur, Na₂SO₄ and on Na₂S with Na₂SO₄ are in duplicates. The individual data point of each replicate is shown as a sphere.

Data Fig. 9). It is, however, drastically different from characterized single-domain assimilatory APS/PAPS reductases, which are thioredoxin/glutathione-dependent. Assimilatory APS/PAPS reductases share no sequence or structural homology with the *M. thermolithotrophicus* enzyme, and several motifs that are proposed to mediate substrate binding and catalytic activity in assimilatory APS/PAPS reductases are absent (Extended Data Fig. 9) (ref. 40).

In *M. thermolithotrophicus*, the α subunit, containing the flavin adenine dinucleotide (FAD), is a member of the fumarate reductase family^{37,41,42} and the β subunit is mainly composed of a ferredoxin-like domain in which two [4Fe-4S] clusters are coordinated by eight cysteine residues (Fig. 4c). While there are no assimilatory P/APSR homologues to *M. thermolithotrophicus* enzyme, it shares 38% sequence identity with the α subunit of the dissimilatory APS reductase from *A. fulgidus* (AfAPSR PDB: 2FJA, rmsd of 1.02 Å for 437 C α aligned on the α subunit). The residues coordinating APS, invariable in the dissimilatory family, differ in *M. thermolithotrophicus* and might provoke a switch of specificity from APS to PAPS. Despite a short soak with PAP, the putative substrate pocket contains only solvent, and we used the AfAPSR to artificially model PAPS in the active site of the enzyme (Fig. 4d,e). The different substitutions mainly carried by loop 104–123 would accommodate the additional 3'-phosphate group by salt-bridge

interactions and hydrogen bonds (Fig. 4d–f). In APS reductases, however, a conserved glutamine (α 145 in *A. fulgidus*) would clash with this phosphate group. The catalytic residues proposed in dissimilatory APS reductases are retained in the enzyme of *M. thermolithotrophicus* (Extended Data Fig. 9 and Supplementary Fig. 7). We therefore propose an identical reaction mechanism on the basis of a nucleophilic attack of the atom N5 of FAD on the sulfur PAPS, which creates a FAD-PAPS intermediate that decays to PAP and FAD-SO₃²⁻ (refs. 37,42). Taking together the enzyme rates and the structural analysis, we propose that *M. thermolithotrophicus* harbours a unique class of PAPS reductase (MtPAPSR) used to convert PAPS into SO₃²⁻ and PAP.

F₄₂₀-dependent sulfite reductase catalyses the last step of the pathway

The SO₃²⁻ generated by MtPAPSR must be further reduced to HS⁻. In hydrogenotrophic methanogens, SO₃²⁻ damages the methanogenesis-generating machinery and must be detoxified by the F₄₂₀-dependent sulfite reductase (Fsr)^{23,43}. We previously identified and characterized Group I Fsr in *M. thermolithotrophicus* (MtFsr) and determined a robust enzymatic activity towards SO₃²⁻ (ref. 23). Besides a second Fsr isoform, *M. thermolithotrophicus* does not contain other potential sulfite reductases. While mass spectrometry confirmed that the Fsr isolated from SO₄²⁻-grown cells is the characterized Group I MtFsr, the physiological role of the second Fsr isoform remains unknown²³. Therefore, MtFsr is the best candidate to catalyse the final reduction of SO₃²⁻ to HS⁻. Native polyacrylamide gel electrophoresis (native PAGE) with cell extracts of cultures grown on different sulfur substrates confirmed the absence of MtFsr from cells grown on Na₂S and its high abundance in cells grown on SO₃²⁻ (refs. 23,43).

We determined a specific sulfite reductase activity of 18.42 ± 0.13 μ mol of oxidized MV min⁻¹ mg⁻¹ of cell extract from Na₂SO₃-grown cells, in comparison to 7.31 ± 0.63 μ mol of oxidized MV min⁻¹ mg⁻¹ of cell extract from Na₂SO₄-grown cells, whereas cell extract from an Na₂S-grown culture had a specific sulfite reductase activity of 3.04 ± 0.25 μ mol of oxidized MV min⁻¹ mg⁻¹ (Fig. 5a). In agreement, we observed a band compatible with Fsr on the native PAGE for the SO₄²⁻-grown culture but in lower amounts compared with SO₃²⁻ conditions (Fig. 5b). The MtFsr structure recently published by our group was obtained from SO₄²⁻-grown cells, which confirmed that it is the same enzyme expressed as under SO₃²⁻ conditions²³. Taken together, these results argue that MtFsr is used as the last enzyme in the SO₄²⁻ reduction pathway (Fig. 5c).

Genetic potential is not enough to sustain SO₄²⁻ growth

Methanogens commonly use HS⁻ as a sulfur source, and the ones that express Fsr type I can also grow on SO₃²⁻ (refs. 13,23,43). Interestingly, some methanogens have genes that encode for proteins of the complete or partial SO₄²⁻ reduction pathway (Supplementary Fig. 8) (ref. 13). So why is *M. thermolithotrophicus* the only methanogen so far that has been proven to grow on SO₄²⁻? We used *Methanocaldococcus infernus* as a model organism to investigate this further. *M. infernus* is a marine hyperthermophile that shares a very similar physiology with *M. thermolithotrophicus* and can grow in the same medium. It contains all genes coding for the enzymes characterized in this study except for the described PAPS. However, the *M. infernus* genome encodes for a putative thioredoxin-dependent PAPS and APSR, which share high sequence identities with the biochemically characterized assimilatory APSR and PAPS from *M. jannaschii* (Fig. 6a and Extended Data Fig. 7b) (refs. 44,45). Therefore, based on genomic information, *M. infernus* should be able to assimilate SO₄²⁻.

M. thermolithotrophicus and *M. infernus* were grown in the same medium and under the same cultivation conditions except that *M. infernus* was kept at 75 °C and *M. thermolithotrophicus* at 65 °C. *M. infernus* grew on 2 mM Na₂S and Na₂SO₃ but was unable to use SO₄²⁻ as a sole source of sulfur in contrast to *M. thermolithotrophicus* (Fig. 6b).

This raises the question about the physiological function of the genes related to SO_4^{2-} assimilation in methanogenic archaea. Based on our data, it could be that other methanogens still require these enzymes to acquire sulfur via the route 1c (Extended Data Fig. 1). The sulfur group would be transferred to an acceptor by a non-canonical sulfo-transferase, which might be important for uncharted biosynthetic pathway(s). This could explain why the gene coding for the PAPP is still present in methanogens also harbouring the genes encoding an ATPS as well as an APSK. A counterargument to this hypothesis is the presence of the thioredoxin-dependent PAPS or APSR, characterized in *M. jannaschii*, which rather argues for route 1b (refs. 13,44,45). It is worth noting that the gene coding for this putative assimilatory APSR also exists in *M. thermolithotrophicus* (WP_018154242.1). Therefore, further biochemical investigations will be needed to elucidate the physiological roles of these enzymes in methanogens.

Discussion

This work unveiled the unique SO_4^{2-} -assimilation metabolism of a methanogenic archaeon, offering a molecular snapshot of the complete set of enzymes involved in the pathway. *M. thermolithotrophicus* activates SO_4^{2-} by conventional ATPS and APSK, but transforms it further by uncanonical enzymes (Fig. 5c).

PAPS produced by the APSK is usually metabolized by thioredoxin- or glutathione-dependent assimilatory PAPS reductases, which are organized as homo-oligomers. In contrast, *MtPAPSR* inherited the heterotetrameric organization and FAD-based catalytic mechanism from dissimilatory APS reductases (Fig. 4, and Extended Data Figs. 1 and 9). We propose that the substitution of only a few amino acids switched the specificity towards PAPS (Fig. 4d–f), which might have been the result of a fine-tuned evolutionary adaptation to promote assimilatory SO_4^{2-} reduction. It would be worthwhile to exchange the residues that confer PAPS traits at the active site (Ser122, Lys120, Arg121) with those of APSR and observe the effects on substrate affinity.

The generated PAP is efficiently hydrolysed by *MtPAPP*. This PAP phosphatase belongs to the DHH family of phosphoesterases and shares structural homology with exonucleases but has no sequence homology with them. In comparison, conventional PAP phosphatases (part of the FIG superfamily) have a different fold (that is, CysQ) and use three magnesium ions to hydrolyse the 3'-phosphate of PAP³⁰. *MtPAPP* appears to be a remarkable example of convergent evolution, illustrating how archaea developed their own apparatus to detoxify PAP efficiently.

Group I Fsr catalyses the final step of the SO_4^{2-} reduction pathway. This enzyme shows distinct traits of dissimilatory sulfite reductases, with the active site composition of an assimilatory one²³. By encoding the *fsr* gene on a different locus and most probably under a different regulator for its expression (for example, sulfite sensor), the methanogen is able to uncouple rapid SO_3^{2-} detoxification from expressing the whole SO_4^{2-} assimilation machinery. While the *MtATPS*, *MtAPSK* and *MtPAPSR* show rather slow catalytic rates (see Supplementary Discussion), *MtFsr* and the *MtPAPP* have high specific activities compared with the first steps, triggering the equilibrium towards HS^- production and efficiently eliminating toxic intermediates. Although our proposed pathway (Fig. 5c) would allow favourable thermodynamics, the first reactions should be regulated to avoid unnecessary ATP hydrolysis. We suspect that *MtATPS*, *MtAPSK* and *MtPAPSR* are cross-regulated by the accumulation of their own products, as already shown for homologues^{39,46,47}, which would allow direct retro-control to harmonize the intracellular sulfur flux.

M. thermolithotrophicus lives at the thermodynamic limit of life but the described SO_4^{2-} assimilation requires the hydrolysis of three ATP to ADP for one processed SO_4^{2-} . Nevertheless, it is expected that under natural conditions, the benefit of fixing SO_4^{2-} counterbalances the energy expenditure. The SO_4^{2-} -grown cultures are not hampered

by the additional energy requirement, which can be explained by our cultivation conditions that provide a high and constant H_2 partial pressure. Under environmental conditions, with a lower and fluctuating H_2 partial pressure, growth on SO_4^{2-} is likely to be more challenging for *M. thermolithotrophicus*. While the methanogen cannot avoid the ATP investment, it may have found an energy-saving strategy for the 8-electron reduction reaction from PAPS to HS^- . Fsr oxidizes F_{420}H_2 , which is reduced back by the F_{420} -reducing hydrogenase^{23,48}. F_{420}H_2 or NAD(P)H would be advantageous electron donors for *MtPAPSR*, but it would require the assistance of an oxidase partner that has not yet been identified. Alternatively, the standalone *MtPAPSR* may depend on reduced ferredoxin, which could be obtained from the H_2 -dependent ferredoxin reduction via the Eha/Ehb complex, another advantageous strategy of hydrogenotrophs to provide reducing power to fuel anabolic reactions (proposed in Fig. 5c) (ref. 49).

So far, it appears that the concomitant process of methanogenesis and complete SO_4^{2-} reduction to HS^- is restricted to *M. thermolithotrophicus*. Strikingly, the only apparent difference between *M. thermolithotrophicus* and other methanogens with the genomic potential to perform SO_4^{2-} reduction is the acquisition of a PAPS reductase, which appears to belong to the dissimilatory family (Supplementary Fig. 8, Extended Data Fig. 7b and Supplementary Discussion). The physiological function of these SO_4^{2-} -reduction-associated genes in other methanogens remains to be uncovered, as well as the advantages of assimilating SO_4^{2-} for *M. thermolithotrophicus*. From an ecological point of view, it might be beneficial, if not essential, for *M. thermolithotrophicus* survival to be able to switch from H_2S uptake to SO_4^{2-} reduction under environmental conditions (see Supplementary Discussion).

The transplantation of the *M. thermolithotrophicus* SO_4^{2-} reduction system into methanogenic hosts, which are already used as gas converters (for example, *Methanothermobacter*), would circumvent the need for highly toxic and explosive H_2S by using inexpensive and abundant SO_4^{2-} . Beyond opening fantastic possibilities for safer biotechnological applications, a SO_4^{2-} -reducing hydrogenotrophic methanogen also reinforces the question about the extent of an intertwined methanogenesis and sulfate reduction pathway during the evolution of early archaea. *M. thermolithotrophicus* has most probably assembled the entire SO_4^{2-} reduction pathway progressively via a 'mix-and-match' scenario, providing a competitive advantage under fluctuating sulfur-source conditions and expanding its ecological niches.

Methods

Archaea strains and cultivation media

M. thermolithotrophicus (DSM 2095), *M. infernus* (DSM 11812) and *A. fulgidus* (DSM 4304) cells were obtained from the Leibniz Institute DSMZ-German Collection of Microorganisms and Cell Cultures (Braunschweig, Germany). *M. thermolithotrophicus* and *M. infernus* were cultivated in the same previously described minimal medium with some modifications²³ (see Extended Data for the complete composition of the media).

Anaerobic growth of Archaea

Cell growth was followed spectrophotometrically by measuring the OD_{600} . The purity of the culture was checked by light microscopy. The methanogens were cultivated with 1×10^5 Pa of $\text{H}_2:\text{CO}_2$ at an 80:20 ratio in the gas phase. *M. infernus* was cultivated at 75 °C in 250 ml glass serum flasks and *M. thermolithotrophicus* was grown at 65 °C in flasks or fermenters. The serum flasks were not shaken but standing. *A. fulgidus* was cultivated in anaerobic and sealed 22 ml Hungate tubes, with 0.8×10^5 Pa $\text{N}_2:\text{CO}_2$. DSM 4304 culture (0.5 ml) was grown in 10 ml of classic media (see Supplementary Materials for the complete composition of the media composition) containing a final concentration of 20 mM D/L-lactate. The culture was incubated at 80 °C, standing. All cultures were stored at room temperature in the dark under anaerobic conditions. For the *A. fulgidus* medium, we found that high molybdate

concentrations made it unstable. One of the bottles with a high MoO_4^{2-} concentration turned yellow (unrelated to O_2 contamination) and was omitted, resulting in triplicate instead of quadruplicate cultures (Fig. 1c, right panel).

Adaptation of *M. thermolithotrophicus* to SO_4^{2-} and minimal SO_4^{2-} requirement

M. thermolithotrophicus cells grown on 2 mM Na_2S were successively transferred to 10 ml sulfur-free cultivation medium. After two transfers, the carry-over sulfur concentration of the inoculum did not support growth of *M. thermolithotrophicus*. By supplementing 2 mM Na_2SO_4 , *M. thermolithotrophicus* growth was resumed. No reducing agent was added to cope with the absence of HS^- , which normally establishes a suitable reducing environment. Incubation without shaking is particularly important for reproducibility. Therefore, after inoculation, the cultures were incubated at 65 °C, standing for one night followed by shaking at 180 revolutions per minute (r.p.m.) until they reached their maximum OD_{600} . The gas phase was refreshed after the overnight incubation to maintain the pressure at 1×10^5 Pa of $\text{H}_2:\text{CO}_2$. To measure the minimal SO_4^{2-} concentration required to sustain growth, sulfur-limited *M. thermolithotrophicus* cells (using an inoculum to medium ratio of 1:20) were provided with 2 mM, 1 mM, 0.5 mM, 0.25 mM, 0.1 mM and 0.04 mM Na_2SO_4 . Growth was still observable for cells grown on 0.1 mM but not on 0.04 mM Na_2SO_4 .

SO_4^{2-} measurements via ion chromatography

Ion chromatography (Methrom ion chromatograph) was used to measure the SO_4^{2-} concentrations, analysed via the software IC MagIC Net 3.2. A volume of 8 ml per sample was required, with a maximum concentration of 0.5 mM SO_4^{2-} . SO_4^{2-} -reducing *M. thermolithotrophicus* cells were therefore grown in 1 l Duran bottles with 100 ml sulfur-free media, which was supplemented with 0.5 mM SO_4^{2-} before inoculation. As a negative control, 0.5 mM Na_2S -grown *M. thermolithotrophicus* cells were used, inoculated and collected similarly as the SO_4^{2-} -reducing cultures. All samples were taken aerobically and were passed through a 0.45 μm filter (Sartorius). If the cell densities were too high to be filtered, the samples were centrifuged at $13,000 \times g$ for 7 min at 4 °C and the supernatant was taken for ion chromatography measurements. The samples were stored at 4 °C if the measurements were not immediately performed.

Growth of *M. thermolithotrophicus* in a fermenter

M. thermolithotrophicus was grown in three independent fermenters at 60 °C, with 10 mM Na_2SO_4 as sole sulfur source. For each fermenter, 7 l of anaerobic cultivation medium (see Sulfur-free cultivation medium for *Methanococcales*) supplemented with 10 mM Na_2SO_4 was continuously bubbled with $\text{H}_2:\text{CO}_2$ (80:20, 3 l min^{-1}). Under stirring (220 r.p.m.), the medium was inoculated with 360 ml preculture (with an OD_{600} higher than 3). One hour after inoculation, the culture was stirred at 800 r.p.m. NaOH (1 M) was used as a base to readjust the pH upon acidification, which was controlled using a pH probe. The cells were grown until late exponential phase (OD_{600} of 6.25–6.8) and then immediately transferred in an anaerobic tent ($\text{N}_2:\text{CO}_2$ atmosphere at a ratio of 90:10). Cells were collected by anaerobic centrifugation for 30 min at $6,000 \times g$ at 4 °C. The highest $\text{OD}_{600\text{nm}}$ recorded for *M. thermolithotrophicus* in a SO_4^{2-} -grown fermenter was 6.8 after 20 h. SO_4^{2-} Culture (7 l) with an OD_{600} of 6.8 yielded 54 g of cells (wet weight). The cell pellet was transferred in a sealed bottle, gassed with 0.3×10^5 Pa N_2 , flash frozen in liquid N_2 and stored at -80 °C.

Synthetic gene constructs

The DNA sequences of the ATP sulfurylase, the APS kinase, the PAP phosphatase and the PAPS reductase α and β subunits from *M. thermolithotrophicus* were codon optimized for *E. coli*, synthesized and cloned into pET-28a(+) vectors. For *MtATPS*, *MtAPSK* and

MtPAPP, the restriction sites *NdeI* and *BamHI* were used, with a stop codon (TGA) incorporated before *BamHI*. For *MtPAPSR*, a His-tag was placed at the C terminus of the α subunit and a ribosome binding site was inserted between the coding sequences of the α and β subunits. The *MtPAPSR* construct had the restriction sites *NcoI* and *BamHI*, with one stop codon incorporated after the His-tag for the α subunit and one stop codon before *BamHI* for the β subunit. These steps were performed by GenScript (GenScript). All sequences used are detailed in Supplementary Information under Constructs and gene codon optimization.

Enzyme overexpression and purification

All constructs were overexpressed and purified under aerobic conditions following a similar protocol, except for *MtPAPSR* which was overexpressed and purified under an anaerobic atmosphere. All enzymes were passed on a HisTrap high-performance column (GE Healthcare), followed, if necessary, by tag cleavage and gel filtration (see Supplementary Materials for the complete protocol).

Protein crystallization

Purified *MtATPS*, *MtAPSK* and *MtPAPP* were kept in 25 mM Tris/HCl pH 7.6, 10% v/v glycerol, 2 mM dithiothreitol and 150 mM NaCl. *MtPAPSR* was kept in the same buffer without NaCl. Freshly prepared unfrozen samples were immediately used for crystallization. *MtATPS*, *MtAPSK* and *MtPAPP* crystals were obtained under aerobic conditions at 18 °C. *MtPAPSR* crystals were obtained anaerobically ($\text{N}_2:\text{H}_2$, gas ratio of 97:3) by initial screening at 20 °C. The sitting drop method was performed on 96-well MRC 2-drop crystallization plates in polystyrene (SWISSCI) containing 90 μl of crystallization solution in the reservoir.

Crystallization of *MtATPS*

MtATPS (0.7 μl) at a concentration of 14 mg ml^{-1} (*MtATPS* form 1, Extended Data Table 1) or at a concentration of 27 mg ml^{-1} (*MtATPS* form 2) was mixed with 0.7 μl reservoir solution. *MtATPS* at 27 mg ml^{-1} was co-crystallized with 2 mM AMPcPP as well as 2 mM Na_2SO_4 . For *MtATPS* form 1, transparent star-shaped crystals appeared after a few weeks in the following crystallization condition: 35% w/v pentaerythritol ethoxylate (15/4 EO/OH) and 100 mM 2-(*N*-morpholino)ethanesulfonic acid (MES) pH 6.5. For *MtATPS* form 2, transparent, long but thin plate-shaped crystals appeared after a few weeks in the following crystallization condition: 20% w/v polyethylene glycol 8000, 100 mM MES pH 6.0 and 200 mM calcium acetate.

Crystallization of *MtAPSK*

MtAPSK (0.7 μl) at a concentration of 17.6 mg ml^{-1} was mixed with 0.7 μl reservoir solution and co-crystallized with 2 mM MgCl_2 . Transparent, plate-shaped crystals appeared after a few weeks in the following crystallization condition: 20% w/v polyethylene glycol 3350 and 100 mM tri-sodium citrate pH 5.5. *MtAPSK* was also crystallized with 2 mM MgCl_2 and 2 mM APS but the obtained structures of those crystals were of lower resolution and without any substrate or product present in the active site.

Crystallization of *MtPAPSR*

MtPAPSR (0.7 μl) at a concentration of 20 mg ml^{-1} was mixed with 0.7 μl reservoir solution and co-crystallized with FAD (0.5 mM final concentration). The crystal used for phasing was a brown flat square and appeared after a few days in the following crystallization condition: 40% v/v 2-methyl-2,4-pentanediol and 100 mM Tris/HCl pH 8.0.

The crystal used to refine at high resolution was brown with an elongated plate shape. It appeared after a few days in the following crystallization condition: 35% v/v 2-methyl-2,4-pentanediol, 100 mM Tris pH 7.0 and 200 mM NaCl. Before transfer to liquid N_2 , the crystal was soaked in 10 mM disodium 3'-phosphoadenosine 5'-phosphate for 7 min.

Crystallization of *MtPAPP*

MtPAPP (0.7 μl) at a concentration of 20 mg ml^{-1} was mixed with 0.7 μl reservoir solution and co-crystallized with Tb-Xo4 (10 mM final concentration), MnCl_2 (2 mM final concentration) and 2 mM PAP. The Tb-Xo4 is a nucleating/phasing agent⁵⁰, which should increase the crystallization performance; however, in this case, the same crystalline form was obtained in the absence of the compound and diffracted to similar resolution. Transparent, bipyramid crystals appeared after a few weeks in the following crystallization condition: 1.6 M tri-sodium citrate.

X-ray crystallography and structural analysis

MtPAPSR crystal handling was done inside the Coy tent under anaerobic atmosphere ($\text{N}_2:\text{H}_2$, 97:3); the other crystals were handled under aerobic conditions. The crystals were directly plunged in liquid nitrogen or were soaked for 5–30 s in their crystallization solution supplemented with a cryoprotectant before being frozen in liquid nitrogen. For *MtATPS* form 2, 30% glycerol was used as cryoprotectant. For *MtAPSK*, 25% ethylene glycol was used as cryoprotectant.

Crystals were tested and collected at 100 K at different synchrotrons (Extended Data Table 1). Data were processed with autoPROC⁵¹ except for *MtPAPP*, which gave better statistics with indexation by the X-ray Detector Software (XDS) and the scaling step performed with SCALA⁵². All data collection statistics are provided in Extended Data Table 1. *MtATPS* forms 1 and 2, *MtAPSK* and *MtPAPP* were solved by using PHENIX with the following templates: 1V47 (ATPS from *T. thermophilus*) for *MtATPS* form 1, *MtATPS* form 1 for *MtATPS* form 2 and 5CB6 (APS kinase from *Synechocystis* sp.) for *MtAPSK*. For *MtPAPP*, the template was created de novo using AlphaFold 2 (ref. 32).

For *MtPAPSR*, an X-ray fluorescence spectrum on the Fe K-edge was measured to optimize the data collection at the appropriate wavelength. Datasets were collected at 1.73646 Å for the single-wavelength anomalous dispersion experiment. Native datasets were collected at a wavelength of 0.97625 Å on another crystal. Data were processed and scaled with autoPROC⁵¹. Phasing, density modification and automatic building were performed with CRANK-2 (ref. 53).

All models were manually rebuilt with COOT and further refined with PHENIX^{54,55}. During the refinement, non-crystallographic symmetry and translational-libration screw were applied. For all structures except for ATPS form 1, hydrogens were added in riding position in the last refinement cycle. Hydrogens were removed in the final deposited models.

All models were validated using MolProbity⁵⁶. Data collection and refinement statistics, as well as PDB identification codes for the deposited models and structure factors are listed in Extended Data Table 1. Figures were generated with PyMOL (Schrödinger). The metal in *MtATPS* was modelled as zinc using CheckMyMetal⁵⁷.

High-resolution clear native PAGE (hrCN PAGE)

To visualize the expression levels of *MtFsr* when cells were grown on different sulfur sources, hrCN PAGE was performed. *M. thermolithotrophicus* cultures (2 \times 10 ml) were supplemented with either 2 mM Na_2S , 2 mM Na_2SO_3 , 2 mM Na_2S and 2 mM Na_2SO_4 , or 2 mM Na_2SO_4 as sulfur substrates and grown for one night at 65 °C, standing. Cells were collected by anaerobic centrifugation at 6,000 $\times g$ for 20 min at room temperature and the cell pellets were resuspended in 2 ml lysis buffer (50 mM tricine pH 8.0 and 2 mM sodium dithionite). The cells were sonicated 4 \times at 70% intensity for 10 s, followed by a 30 s break (MS 73 probe, SONOPULS Bandelin). The hrCN PAGE was run anaerobically and the protocol is detailed in Extended Data under hrCN PAGE preparation. One gel with an 8–15% acrylamide gradient was run (shown in Fig. 5b) and another one with a 5–15% acrylamide gradient (see Source Data Fig. 5).

Coupled enzyme activity of *MtATPS*/*MtAPSK*

The activity of both enzymes was determined by the production of ADP which was coupled to NADH oxidation via pyruvate kinase and

lactate dehydrogenase⁵⁸. The assays were performed in a final volume of 100 μl 96-well deep-well plates and spectrophotometrically monitored (Omega multimode microplate reader) at 360 nm at 35 °C. KH_2PO_4 (100 mM) at pH 7.0, supplemented with 1.5 mM MgCl_2 and 100 mM KCl, was used as a buffer. For NADH, a molar extinction coefficient of 4,546.7 $\text{cm}^{-1}\text{M}^{-1}$ was experimentally determined for the above-named conditions. To the buffer, 1 mM NADH, 2.5 mM Na_2SO_4 , 1 mM phosphoenolpyruvate (PEP), 2 mM ATP, 2 U inorganic pyrophosphatase (*Saccharomyces cerevisiae*, 10108987001, Sigma-Aldrich), 1.1 U ml^{-1} lactate dehydrogenase, 0.8 U ml^{-1} pyruvate kinase (rabbit muscle, P0294, Sigma-Aldrich) and 0.5 mg ml^{-1} *MtAPSK* (all final concentrations) were added. The reaction was started by the addition of 0.5 mg ml^{-1} *MtATPS*. Addition of 0.02 mM Na_2MoO_4 did not affect activity (0.116 ± 0.027 μmol of oxidized NADH $\text{min}^{-1}\text{mg}^{-1}$), but the addition of 2 mM Na_2MoO_4 resulted in a decrease (0.068 ± 0.019 μmol of oxidized NADH $\text{min}^{-1}\text{mg}^{-1}$). All assays were performed in triplicates.

MtPAPP enzyme assay

The activity of the *MtPAPP* was determined by the production of orthophosphate, which was quantified using the malachite green phosphate assay kit (Sigma-Aldrich) by the formation of a green complex. The assays were performed in 96-well deep-well plates and the absorbance at 620 nm was spectrophotometrically followed (Omega multimode microplate reader). Tris/HCl (25 mM) at pH 7.64 was used as a buffer. Buffer, 40 μM PAP or 90 μM of AMP/ADP/ATP/APS or PP_i, 1 mg ml^{-1} bovine serum albumin, 50 μM MnCl_2 and/or 50 μM MgCl_2 (final concentration) were mixed in a 1.5 ml Eppendorf tube on ice. Previously frozen *MtPAPP* (0.5 $\mu\text{g ml}^{-1}$ final concentration) was added and the mixture (final volume of 40 μl) was immediately incubated for 5 min at 40 °C. Next, 14 μl of the reaction mix was diluted in 66 μl of filtered Milli-Q H_2O and immediately flash frozen in liquid N_2 to quench the reaction. Then, 20 μl of malachite green reagent was added to the samples, the mixture was incubated at room temperature for 30 min and the formation of the green complex was measured at 620 nm. All assays were performed in triplicates. The measurements presented in Fig. 3a come from two different experiments (left and right subpanels). Both experiments were performed at two different days with the same enzyme preparation.

Coupled *MtPAPSR* assay

Since PAPS is unstable at high temperatures, we first tried to determine the activity of *MtPAPSR* in the direction of PAPS production, as previously described for dissimilatory APS reductases for APS production³⁸. PAPS oxidation was determined in 50 mM Tris/HCl buffer (pH 7.5) containing 5 mM Na_2SO_3 , 2 mM PAP or 2 mM AMP (final concentrations) and 3.27 $\mu\text{g ml}^{-1}$ *MtPAPSR*. The reaction was started with a final concentration of 0.5 mM $\text{K}_3\text{Fe}(\text{CN})_6$. The decrease in absorbance at 420 nm was measured and corrected for the background reaction without enzyme. No activity was detected. Therefore, we used the physiological reaction to monitor *MtPAPSR* activity. To perform the coupled *MtPAPSR* assay, the enzymes needed to be purified at the same time and immediately used for the assay (see Supplementary Materials for the detailed purification protocol for the enzymes used in this assay).

MtPAPSR activity assays were carried out in an anaerobic atmosphere (100% N_2) at 45 °C. The assays were performed in 200 μl final volume in 96-well deep-well plates and spectrophotometrically monitored on a SPECTROstar Nano microplate reader. HEPES (50 mM, pH 7.0) supplemented with 50 mM KCl, 1.5 mM MnCl_2 and 1.5 mM MgCl_2 was used as a buffer. Reduced methyl viologen (MV_{red} , 0.5 mM) served as an electron donor for *MtPAPSR*. The molar extinction coefficient ($\epsilon_{600\text{nm}} = 8,133.3$ $\text{cm}^{-1}\text{M}^{-1}$) was experimentally determined using the above-named conditions and by reducing methyl viologen with 2 mM sodium dithionite. For the assay, methyl viologen was reduced with carbon monoxide by the CO-dehydrogenase from *Clostridium autoethanogenum* according to a previously published protocol⁵⁹.

CO was exchanged for N₂ and the MV_{red} was immediately used for the assay. To the buffer and MV_{red}, 5 mM ATP, 1 mM sodium dithionite, 0.2 U pyrophosphatase (*E. coli*, MFCD00131379, Sigma-Aldrich), 0.127 mg ml⁻¹ MtATPS, 0.12 mg ml⁻¹ MtAPSK, 0.1 mg ml⁻¹ MtPAPP and 0.0645 mg ml⁻¹ MtPAPSR were added. The reaction was started by the addition of 5 mM Na₂SO₄ and followed by oxidation of MV_{red} at 600 nm. All assays were performed in triplicates.

Sulfite reductase activity in cell extracts

To determine the sulfite reductase activity from *M. thermolithotrophicus*, cultures were grown on either 2 mM Na₂S, 2 mM Na₂SO₃ or Na₂SO₄ in 10 ml of the above-mentioned medium in serum flasks. Cells (9 ml) were collected in late exponential phase (OD₆₀₀: 3.45 for 2 mM Na₂S, 3.91 for 2 mM Na₂SO₃, 3.37 for Na₂SO₄) by centrifugation at 6,000 × g for 10 min at 4 °C. The supernatant was discarded and the cell pellets were frozen in liquid N₂. The pellets were then resuspended in 1 ml 0.5 M KH₂PO₄ pH 7.0. The cells were lysed by sonication (2 × 10 s at 50% intensity, probe MS73, SONOPULS Bandelin), followed by centrifugation at 4 °C at 15,600 × g. The supernatant was passed through a 0.2 μm filter and the protein concentration was determined by the Bradford method (6.63 mg ml⁻¹ for 2 mM Na₂S, 6.14 mg ml⁻¹ for 2 mM Na₂SO₃ and 6.31 mg ml⁻¹ for Na₂SO₄). The activity assays were performed under an anaerobic atmosphere (100% N₂) at 50 °C in 96-well deep-well plates and spectrophotometrically monitored (SPECTROstar Nano microplate reader). The assay mixture contained 0.5 M KH₂PO₄ pH 7.0, 118 μM MV_{red} (final concentration, previously reduced with the equimolar amount of sodium dithionite) and 30 μM Na₂SO₃ (final concentration). Under these conditions, a molar extinction coefficient of ε_{600nm} = 9,840 cm⁻¹ M⁻¹ was experimentally determined. The reaction was started by the addition of 0.05 μg of cell extract, followed by oxidation of MV_{red} at 600 nm. All assays were performed in triplicates.

Phylogenetic trees

For a detailed description of the phylogenetic analysis, see Supplementary Materials⁶⁰.

Reporting summary

Further information on research design is available in the Nature Portfolio Reporting Summary linked to this article.

Data availability

All structures used for structural comparison are accessible from the Protein Data Bank and accordingly cited in the text. The structures were deposited in the Protein Data Bank under the ID: 8A8G for MtATPS form 1, 8A8D for MtATPS form 2, 8A8H for MtAPSK, 8A8K for MtPAPP and 8A8O for MtPAPSR. The data for this study are available in the paper and its Supplementary Information. Source data are provided with this paper.

References

- Perona, J. J., Rauch, B. J. & Driggers, C. M. in *Molecular Mechanisms of Microbial Evolution* (ed Rampelotto, P. H.) 371–408 (Springer, 2018).
- Eser, B. E., Zhang, X., Chanani, P. K., Begley, T. P. & Ealick, S. E. From suicide enzyme to catalyst: the iron-dependent sulfide transfer in *Methanococcus jannaschii* thiamin thiazole biosynthesis. *J. Am. Chem. Soc.* **138**, 3639–3642 (2016).
- Liu, Y., Beer, L. L. & Whitman, W. B. Methanogens: a window into ancient sulfur metabolism. *Trends Microbiol.* **20**, 251–258 (2012).
- Daniels, L., Belay, N. & Rajagopal, B. S. Assimilatory reduction of sulfate and sulfite by methanogenic bacteria. *Appl. Environ. Microbiol.* **51**, 703–709 (1986).
- Payne, D., Spietz, R. L. & Boyd, E. S. Reductive dissolution of pyrite by methanogenic archaea. *ISME J.* **15**, 3498–3507 (2021).
- Huber, H., Thomm, M., König, H., Thies, G. & Stetter, K. O. *Methanococcus thermolithotrophicus*, a novel thermophilic lithotrophic methanogen. *Arch. Microbiol.* **132**, 47–50 (1982).
- Kuivila, K. M., Murray, J. W., Devol, A. H. & Novelli, P. C. Methane production, sulfate reduction and competition for substrates in the sediments of Lake Washington. *Geochim. Cosmochim. Acta* **53**, 409–416 (1989).
- Thauer, R. K., Kaster, A.-K., Seedorf, H., Buckel, W. & Hedderich, R. Methanogenic archaea: ecologically relevant differences in energy conservation. *Nat. Rev. Microbiol.* **6**, 579–591 (2008).
- Kristjansson, J. K. & Schönheit, P. Why do sulfate-reducing bacteria outcompete methanogenic bacteria for substrates? *Oecologia* **60**, 264–266 (1983).
- Deppenmeier, U. & Müller, V. in *Bioenergetics: Energy Conservation and Conversion* (eds Schafer, G. & Penefsky, H. S.) 123–152 (Springer, 2008).
- Hocking, W. P., Stokke, R., Roalkvam, I. & Steen, I. H. Identification of key components in the energy metabolism of the hyperthermophilic sulfate-reducing archaeon *Archaeoglobus fulgidus* by transcriptome analyses. *Front. Microbiol.* **5**, 95 (2014).
- Marietou, A., Roy, H., Jorgensen, B. B. & Kjeldsen, K. U. Sulfate transporters in dissimilatory sulfate reducing microorganisms: a comparative genomics analysis. *Front. Microbiol.* **9**, 309 (2018).
- Yu, H. et al. Comparative genomics and proteomic analysis of assimilatory sulfate reduction pathways in anaerobic methanotrophic archaea. *Front. Microbiol.* **9**, 2917 (2018).
- Ramos, A. R., Keller, K. L., Wall, J. D. & Pereira, I. A. The membrane QmoABC complex interacts directly with the dissimilatory adenosine 5'-phosphosulfate reductase in sulfate reducing bacteria. *Front. Microbiol.* **3**, 137 (2012).
- Oliveira, T. F. et al. The crystal structure of *Desulfovibrio vulgaris* dissimilatory sulfite reductase bound to DsrC provides novel insights into the mechanism of sulfate respiration. *J. Biol. Chem.* **283**, 34141–34149 (2008).
- Santos, A. A. et al. A protein trisulfide couples dissimilatory sulfate reduction to energy conservation. *Science* **350**, 1541–1545 (2015).
- Ellis, R. J. Sulphate activation in higher plants. *Planta* **88**, 34–42 (1969).
- Reuveny, Z. Derepression of ATP sulfurylase by the sulfate analogs molybdate and selenate in cultured tobacco cells. *Proc. Natl Acad. Sci. USA* **74**, 619–622 (1977).
- Biswas, K. C., Woodards, N. A., Xu, H. & Barton, L. L. Reduction of molybdate by sulfate-reducing bacteria. *Biometals* **22**, 131–139 (2009).
- Jesus, E., Lima, L., Bernardez, L. A. & Almeida, P. Inhibition of microbial sulfate reduction by molybdate. *Braz. J. Pet. Gas.* **9**, 95 (2015).
- Zane, G. M., Wall, J. D. & De León, K. B. Novel mode of molybdate inhibition of *Desulfovibrio vulgaris* Hildenborough. *Front. Microbiol.* <https://doi.org/10.3389/fmicb.2020.610455> (2020).
- Zhang, Q., Lee, B.-R., Park, S.-H., Jeong, G.-O. & Kim, T.-H. Molybdate alters sulfate assimilation and induces oxidative stress in white clover (*Trifolium repens* L.). *J. Kor. Soc. Grassl. Forage Sci.* **33**, 153–158 (2013).
- Jespersen, M., Pierik, A. J. & Wagner, T. Structures of the sulfite detoxifying F₄₂₀-dependent enzyme from *Methanococcales*. *Nat. Chem. Biol.* <https://doi.org/10.1038/s41589-022-01232-y> (2023).
- Lampreia, J., Pereira, A. S. & Moura, J. G. in *Methods in Enzymology* Vol. 243 (eds Peck, Jr., H. D. & Le Gall, J.) 241–260 (Academic Press, 1994).
- Parey, K. et al. Structural, biochemical and genetic characterization of dissimilatory ATP sulfurylase from *Allochromatium vinosum*. *PLoS ONE* **8**, e74707 (2013).

26. Beynon, J. D. et al. Crystal structure of ATP sulfurylase from the bacterial symbiont of the hydrothermal vent tubeworm *Riftia pachyptila*. *Biochemistry* **40**, 14509–14517 (2001).
27. Taguchi, Y., Sugishima, M. & Fukuyama, K. Crystal structure of a novel zinc-binding ATP sulfurylase from *Thermus thermophilus* HB8. *Biochemistry* **43**, 4111–4118 (2004).
28. Herrmann, J., Nathin, D., Lee, S. G., Sun, T. & Jez, J. M. Recapitulating the structural evolution of redox regulation in adenosine 5'-phosphosulfate kinase from Cyanobacteria to plants. *J. Biol. Chem.* **290**, 24705–24714 (2015).
29. Ravilious, G. E., Nguyen, A., Francois, J. A. & Jez, J. M. Structural basis and evolution of redox regulation in plant adenosine-5'-phosphosulfate kinase. *Proc. Natl Acad. Sci. USA* **109**, 309–314 (2012).
30. Erickson, A. I., Sarsam, R. D. & Fisher, A. J. Crystal structures of *Mycobacterium tuberculosis* CysQ, with substrate and products bound. *Biochemistry* **54**, 6830–6841 (2015).
31. Dichtl, B., Stevens, A. & Tollervey, D. Lithium toxicity in yeast is due to the inhibition of RNA processing enzymes. *EMBO J.* **16**, 7184–7195 (1997).
32. Jumper, J. et al. Highly accurate protein structure prediction with AlphaFold. *Nature* **596**, 583–589 (2021).
33. Senior, A. W. et al. Improved protein structure prediction using potentials from deep learning. *Nature* **577**, 706–710 (2020).
34. Mechold, U., Fang, G., Ngo, S., Ogrzyzko, V. & Danchin, A. YtqI from *Bacillus subtilis* has both oligoribonuclease and pAp-phosphatase activity. *Nucleic Acids Res.* **35**, 4552–4561 (2007).
35. Schmier, B. J., Nelters, C. M. & Malhotra, A. Structural basis for the bidirectional activity of *Bacillus* nanoRNase NrnA. *Sci. Rep.* **7**, 11085 (2017).
36. Yamagata, A., Kakuta, Y., Masui, R. & Fukuyama, K. The crystal structure of exonuclease RecJ bound to Mn²⁺ ion suggests how its characteristic motifs are involved in exonuclease activity. *Proc. Natl Acad. Sci. USA* **99**, 5908–5912 (2002).
37. Chiang, Y. L. et al. Crystal structure of adenylsulfate reductase from *Desulfovibrio gigas* suggests a potential self-regulation mechanism involving the C terminus of the beta-subunit. *J. Bacteriol.* **191**, 7597–7608 (2009).
38. Fritz, G., Buchert, T. & Kroneck, P. M. The function of the [4Fe-4S] clusters and FAD in bacterial and archaeal adenylsulfate reductases. Evidence for flavin-catalyzed reduction of adenosine 5'-phosphosulfate. *J. Biol. Chem.* **277**, 26066–26073 (2002).
39. Schwenn, J. D. & Schriek, U. PAPS-reductase from *Escherichia coli*: characterization of the enzyme as probe for thioredoxins. *Z. Naturforsch. C. J. Biosci.* **42**, 93–102 (1987).
40. Yu, Z., Lemongello, D., Segel, I. H. & Fisher, A. J. Crystal structure of *Saccharomyces cerevisiae* 3'-phosphoadenosine-5'-phosphosulfate reductase complexed with adenosine 3',5'-bisphosphate. *Biochemistry* **47**, 12777–12786 (2008).
41. Schiffer, A., Fritz, G., Kroneck, P. M. H. & Ermler, U. Reaction mechanism of the iron-sulfur flavoenzyme adenosine-5'-phosphosulfate reductase based on the structural characterization of different enzymatic states. *Biochemistry* **45**, 2960–2967 (2006).
42. Fritz, G. et al. Structure of adenylsulfate reductase from the hyperthermophilic *Archaeoglobus fulgidus* at 1.6-Å resolution. *Proc. Natl Acad. Sci. USA* **99**, 1836–1841 (2002).
43. Johnson, E. F. & Mukhopadhyay, B. A new type of sulfite reductase, a novel coenzyme F₄₂₀-dependent enzyme, from the methanarchaeon *Methanocaldococcus jannaschii*. *J. Biol. Chem.* **280**, 38776–38786 (2005).
44. Cho, M. K. Discovery of Novel 3'-Phosphoadenosine-5'-Phosphosulfate (Paps) Reductase from Methanarchaeon *Methanocaldococcus jannaschii*. MSc thesis, Baylor University (2013).
45. Lee, J. S. et al. Discovery of a novel adenosine 5'-phosphosulfate (APS) reductase from the methanarchaeon *Methanocaldococcus jannaschii*. *Process Biochem.* **46**, 154–161 (2011).
46. Renosto, F., Martin, R. L., Wailes, L. M., Daley, L. A. & Segel, I. H. Regulation of inorganic sulfate activation in filamentous fungi. Allosteric inhibition of ATP sulfurylase by 3'-phosphoadenosine-5'-phosphosulfate. *J. Biol. Chem.* **265**, 10300–10308 (1990).
47. Timothy, O., Carol, C. & Segel, I. H. ATP sulfurylase from higher plants: purification and preliminary kinetics studies on the cabbage leaf enzyme. *Plant Physiol.* **70**, 39–45 (1982).
48. Greening, C. et al. Physiology, biochemistry, and applications of F₄₂₀- and F_o-dependent redox reactions. *Microbiol. Mol. Biol. Rev.* **80**, 451–493 (2016).
49. Lie, T. J. et al. Essential anaplerotic role for the energy-converting hydrogenase Eha in hydrogenotrophic methanogenesis. *Proc. Natl Acad. Sci. USA* **109**, 15473–15478 (2012).
50. Engilberge, S. et al. Crystallophore: a versatile lanthanide complex for protein crystallography combining nucleating effects, phasing properties, and luminescence. *Chem. Sci.* **8**, 5909–5917 (2017).
51. Vonrhein, C. et al. Data processing and analysis with the autoPROC toolbox. *Acta Crystallogr. D* **67**, 293–302 (2011).
52. Winn, M. D. et al. Overview of the CCP4 suite and current developments. *Acta Crystallogr. D* **67**, 235–242 (2011).
53. Pannu, N. S. et al. Recent advances in the CRANK software suite for experimental phasing. *Acta Crystallogr. D* **67**, 331–337 (2011).
54. Emsley, P., Lohkamp, B., Scott, W. G. & Cowtan, K. Features and development of Coot. *Acta Crystallogr. D* **66**, 486–501 (2010).
55. Liebschner, D. et al. Macromolecular structure determination using X-rays, neutrons and electrons: recent developments in Phenix. *Acta Crystallogr. D* **75**, 861–877 (2019).
56. Chen, V. B. et al. MolProbity: all-atom structure validation for macromolecular crystallography. *Acta Crystallogr. D* **66**, 12–21 (2010).
57. Zheng, H. et al. CheckMyMetal: a macromolecular metal-binding validation tool. *Acta Crystallogr. D* **73**, 223–233 (2017).
58. Wayllace, N. Z. et al. An enzyme-coupled continuous spectrophotometric assay for glycogen synthases. *Mol. Biol. Rep.* **39**, 585–591 (2012).
59. Lemaire, O. N. & Wagner, T. Gas channel rerouting in a primordial enzyme: structural insights of the carbon-monoxide dehydrogenase/acetyl-CoA synthase complex from the acetogen *Clostridium autoethanogenum*. *Biochim. Biophys. Acta Bioenerg.* **1862**, 148330 (2021).
60. Tamura, K., Stecher, G. & Kumar, S. MEGA11: molecular evolutionary genetics analysis version 11. *Mol. Biol. Evol.* **38**, 3022–3027 (2021).
61. Robert, X. & Gouet, P. Deciphering key features in protein structures with the new ENDScript server. *Nucleic Acids Res.* **42**, W320–W324 (2014).
62. Edgar, R. C. MUSCLE: a multiple sequence alignment method with reduced time and space complexity. *BMC Bioinformatics* **5**, 113 (2004).

Acknowledgements

We thank the Max Planck Institute for Marine Microbiology and the Max Planck Society for continuous support; the SOLEIL synchrotron for beam time allocation and the beamline staff of Proxima-1 for assistance with data collection; the staff of beamline X06DA from SLS and P11 at PETRA III; D. R. Dean for providing us the RE plasmid pDB1281; C. Probian and R. Appel for continuous support in the Microbial Metabolism laboratory and cultivating *Archaeoglobus fulgidus*; G. Wegener and M. Alisch from the HGF MPG Joint Research

Group for Deep-Sea Ecology and Technology for assistance with the ion chromatography measurements; U. Ermler, J. Fritz-Steuber and G. Fritz for great discussions and critical comments regarding manuscript. This research was funded by the Max-Planck Gesellschaft and the Novo Nordisk foundation (NNF21OC0070790, TW). M.J. was supported by the Deutsche Forschungsgemeinschaft Schwerpunktprogram 1927 “Iron-sulfur for Life” (WA 4053/1-1, M.J.).

Author contributions

M.J. cultivated the methanogens, purified and crystallized all proteins described in this study. M.J. performed all biochemical characterization. M.J. and T.W. collected X-ray data and solved the structures. M.J. and T.W. refined and validated all models. T.W. and M.J. designed the research and wrote the paper.

Funding

Open access funding provided by Max Planck Society.

Competing interests

The authors declare no competing interests.

Additional information

Extended data is available for this paper at <https://doi.org/10.1038/s41564-023-01398-8>.

Supplementary information The online version contains supplementary material available at <https://doi.org/10.1038/s41564-023-01398-8>.

Correspondence and requests for materials should be addressed to Tristan Wagner.

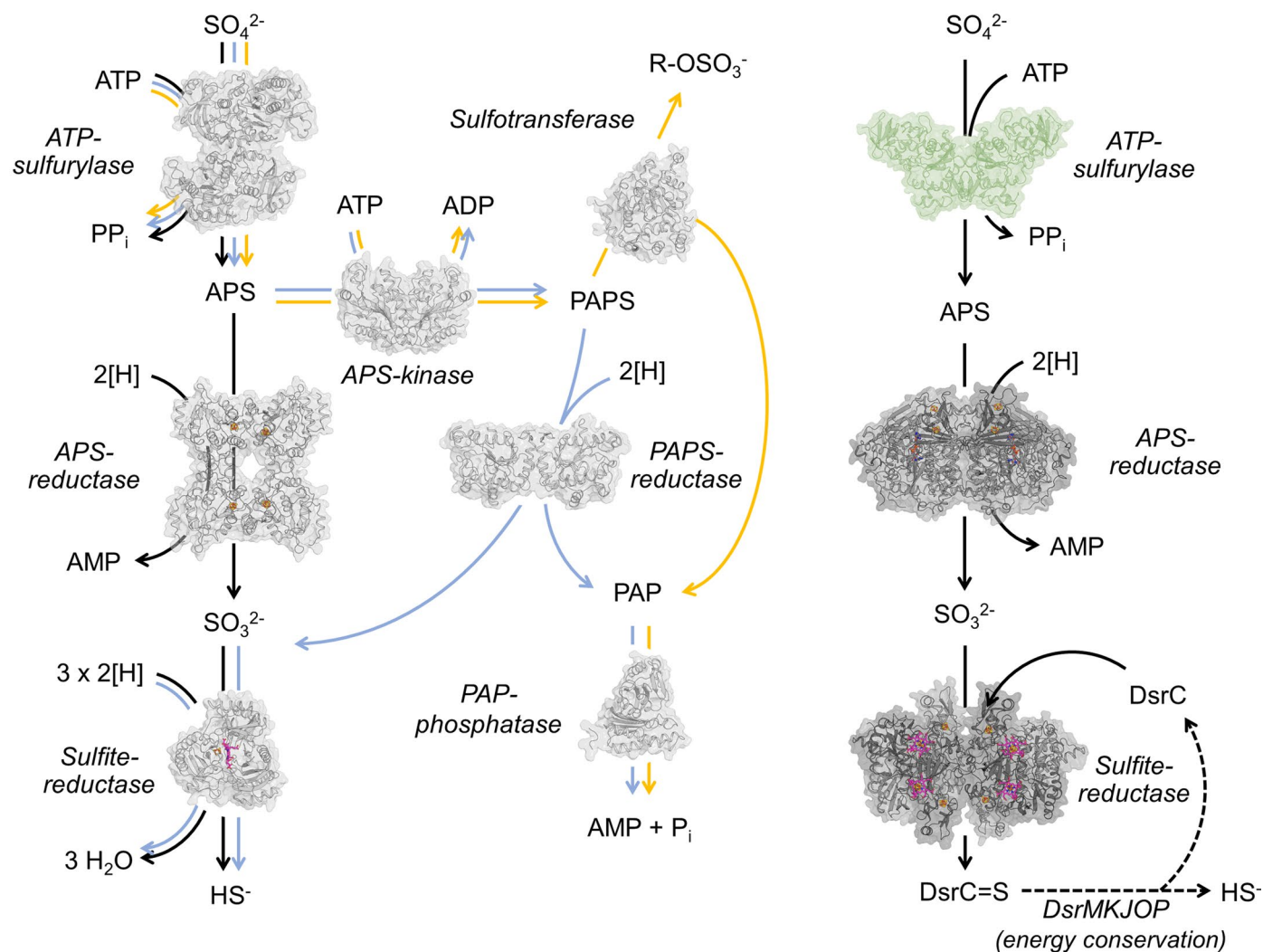
Peer review information *Nature Microbiology* thanks M. Elizabeth Stroupe and the other, anonymous, reviewer(s) for their contribution to the peer review of this work.

Reprints and permissions information is available at www.nature.com/reprints.

Publisher's note Springer Nature remains neutral with regard to jurisdictional claims in published maps and institutional affiliations.

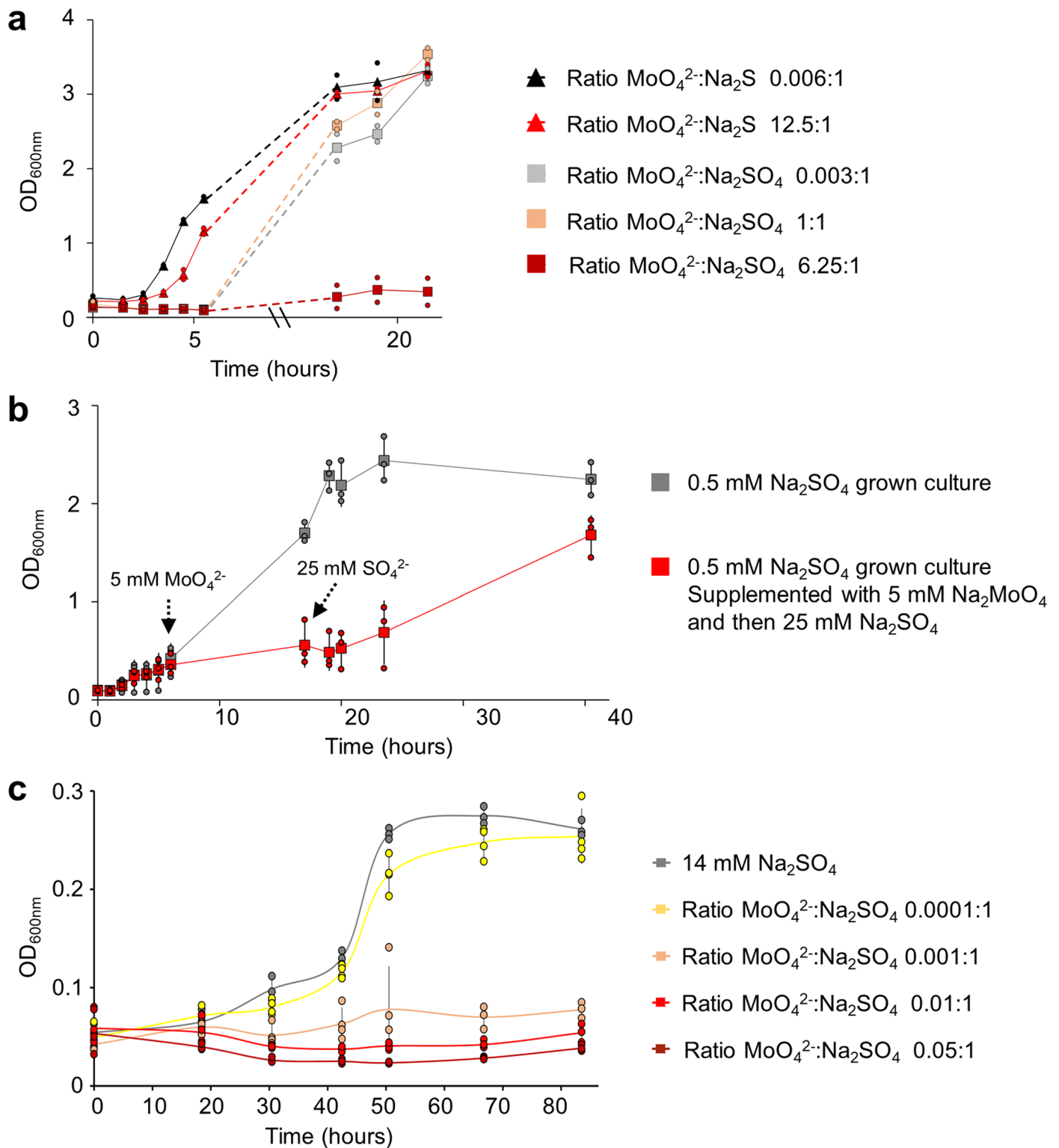
Open Access This article is licensed under a Creative Commons Attribution 4.0 International License, which permits use, sharing, adaptation, distribution and reproduction in any medium or format, as long as you give appropriate credit to the original author(s) and the source, provide a link to the Creative Commons license, and indicate if changes were made. The images or other third party material in this article are included in the article's Creative Commons license, unless indicated otherwise in a credit line to the material. If material is not included in the article's Creative Commons license and your intended use is not permitted by statutory regulation or exceeds the permitted use, you will need to obtain permission directly from the copyright holder. To view a copy of this license, visit <http://creativecommons.org/licenses/by/4.0/>.

© The Author(s) 2023

Assimilatory SO_4^{2-} -reduction (1) Routes: a) b) c)Dissimilatory SO_4^{2-} -reduction (2)

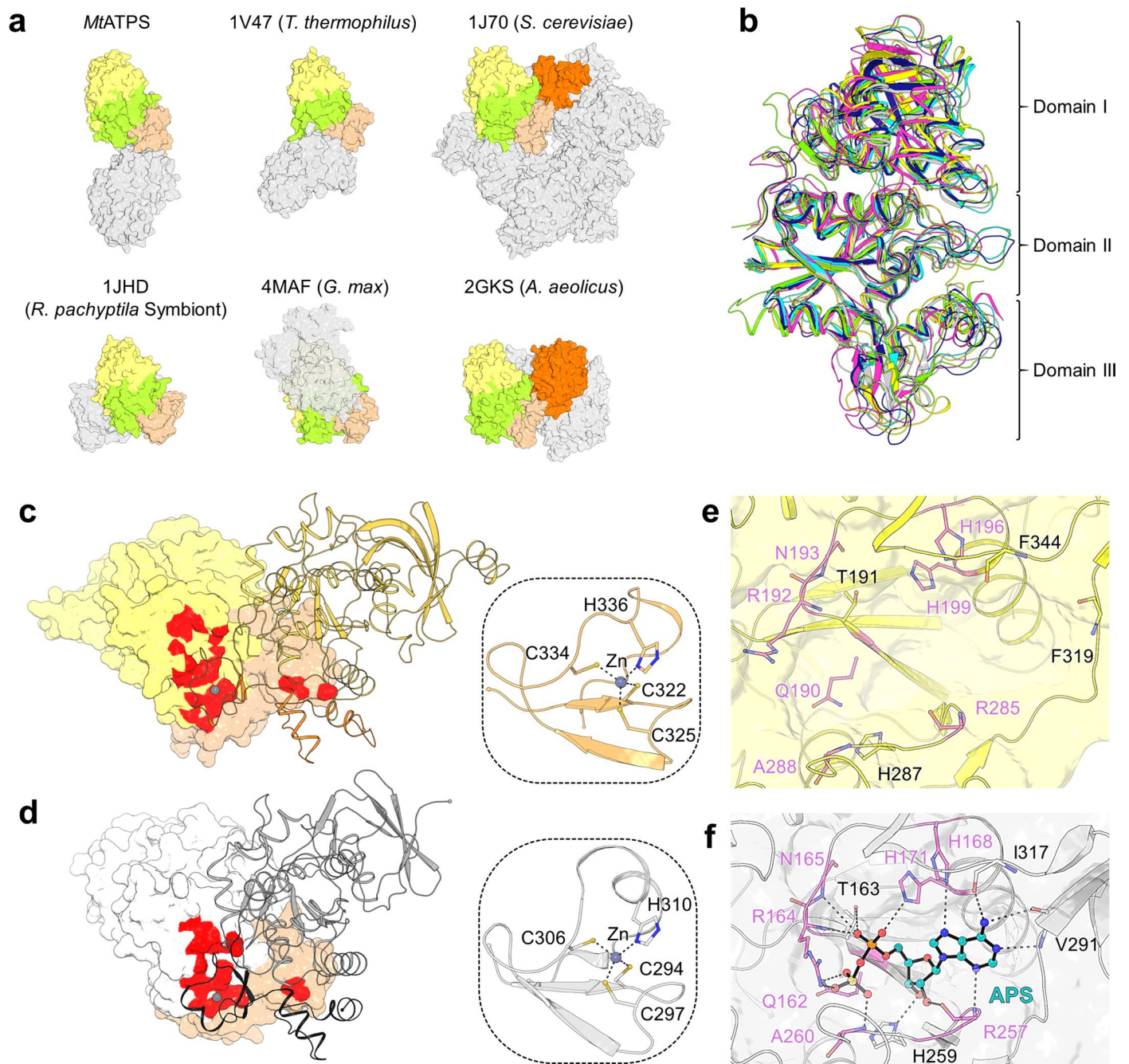
Extended Data Fig. 1 | Sulfate (SO_4^{2-})-reduction pathways. Assimilatory SO_4^{2-} -reduction. (Route 1a, 1b, 1c) SO_4^{2-} is activated by the ATP-sulfurylase (for example *Glycine max*, PDB: 4MAF) to APS. (1a) APS gets directly reduced to sulfite (SO_3^{2-}) and AMP by a one [4Fe-4S]-cluster containing APS-reductase (for example *Pseudomonas aeruginosa*, PDB: 2GOY, thioredoxin dependent). (1b, c) Alternatively, the APS gets further phosphorylated by an APS-kinase (for example *Arabidopsis thaliana*, PDB: 3UIE) to produce PAPS. (1b) A PAPS-reductase (*Saccharomyces cerevisiae*, PDB: 2OQ2, thioredoxin dependent) converts PAPS into SO_3^{2-} and PAP. The PAP will be hydrolysed to inorganic phosphate (P_i) and AMP by a PAP-phosphatase (for example *Mycobacterium tuberculosis*, PDB: 5DJJ). (1a, b) A sulfite-reductase (*Escherichia coli*, PDB: 1AOP) reduces the SO_3^{2-} into S^{2-} , which can then be incorporated into biomass. In the route 1c, a sulfotransferase (for example *A. thaliana*, PDB: 5MEK) catalyses the transfer of the sulfo-group

(R-OSO_3^-) from PAPS to an alcohol or amine acceptor. **Dissimilatory SO_4^{2-} -reduction.** SO_4^{2-} is activated by the ATP-sulfurylase to APS and further reduced to SO_3^{2-} by an APS-reductase (for example *Archaeoglobus fulgidus*, PDB: 2FJA), which contains two [4Fe-4S]-cluster and a FAD. A sulfite-reductase (for example *A. fulgidus*, PDB: 3MM5) reduces the SO_3^{2-} and branches it on the carrier DsrC. The membrane complex DsrMKJOP (for example *Allochrocatium vinosum*) reduces the sulfur into HS^- concomitantly with ion translocation for energy conservation. Sirohemes, FAD and [4Fe-4S]-clusters are represented in sticks and spheres, with carbon, oxygen, nitrogen, sulfur and iron coloured in pink, red, blue, yellow and orange. The enzymes are shown in cartoon and transparent surface in their oligomeric state. The ATPS of *A. fulgidus* was modelled using AlphaFold²³ and coloured in green. The bifunctional ATP-sulfurylase CysDN using an additional GTP, was not presented here to simplify the scheme.



Extended Data Fig. 2 | Impact of Molybdate (MoO_4^{2-}) on SO_4^{2-} -reducing archaea. a, MoO_4^{2-} tolerance of *M. thermolithotrophicus*. The archaeon was grown on SO_4^{2-} (grey square), SO_4^{2-} supplemented with an equimolar amount of MoO_4^{2-} (wheat square) and SO_4^{2-} supplemented with an excess of MoO_4^{2-} (dark red square). As a control, Na_2S grown cultures (S^2 , black triangle) and Na_2S grown cultures with an excess of MoO_4^{2-} (red triangle) were used. This growth experiment was performed in duplicates. b, Effect of $\text{MoO}_4^{2-}:\text{SO}_4^{2-}$ ratios in *M. thermolithotrophicus* cultures grown on 0.5 mM Na_2SO_4 . Grey squares indicate the growth curve of SO_4^{2-} -reducers without addition of MoO_4^{2-} . The red squares

indicate the growth curve of SO_4^{2-} -reducers exposed to 5 mM of MoO_4^{2-} , followed by the addition of 25 mM Na_2SO_4 . Black, dashed arrows indicate time of MoO_4^{2-} and SO_4^{2-} addition. This growth experiment was performed in triplicates. c, *Archaeoglobus fulgidus* sensitivity towards MoO_4^{2-} . Here, a $\text{MoO}_4^{2-}:\text{SO}_4^{2-}$ ratio of 0.001:1 is sufficient to inhibit growth of *A. fulgidus*. The data shown are quadruplicates except for the lowest and the highest $\text{MoO}_4^{2-}:\text{SO}_4^{2-}$ ratio, which were performed in triplicates. All experiments are represented as data mean and for b, \pm standard deviation (s.d.).



Extended Data Fig. 3 | ATP-sulfurylase of *M. thermolithotrophicus* (*MtATPS*).

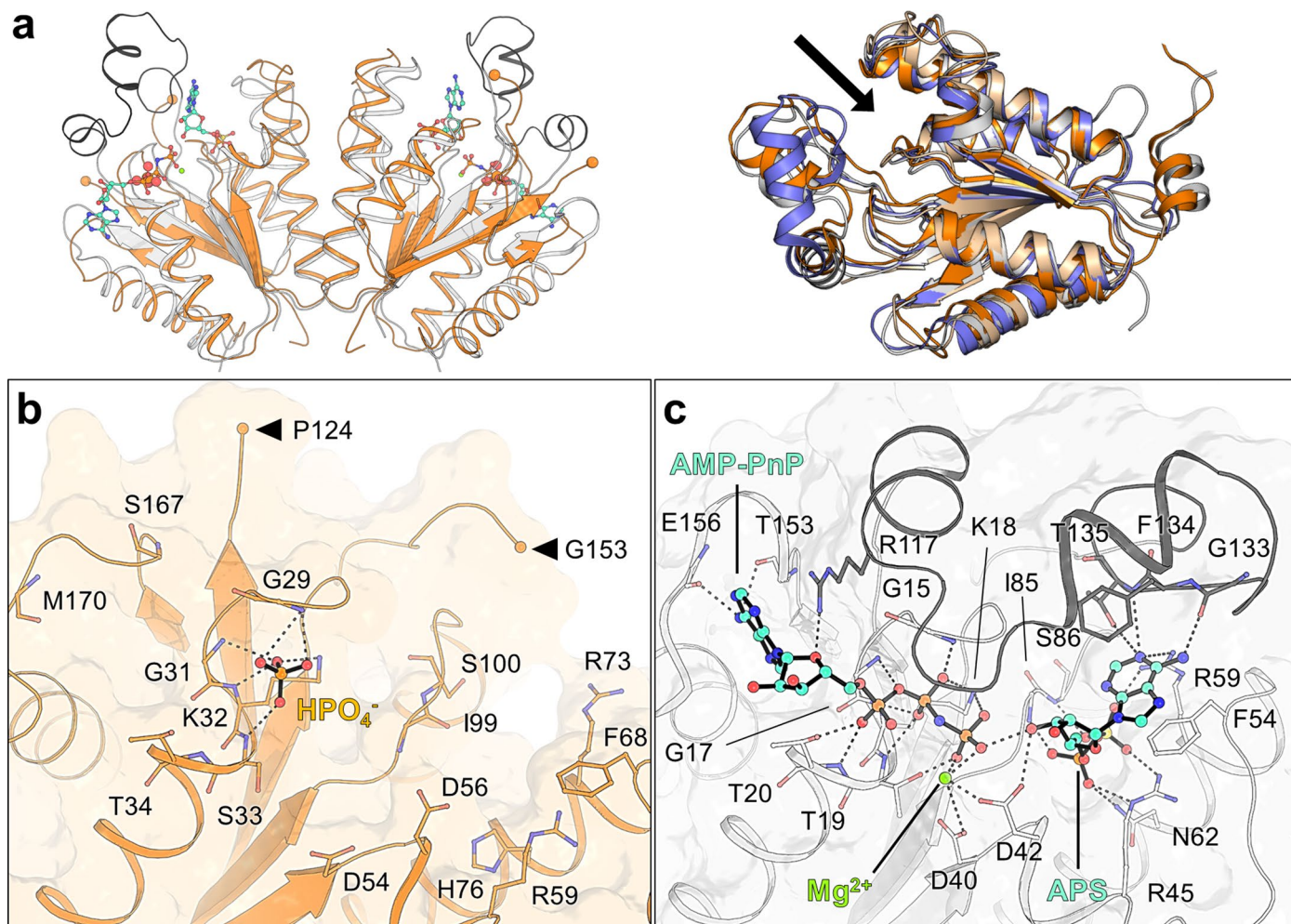
a, Comparison of ATPase in surface representation, coloured by the domain composition I (yellow), II (light green), III (wheat) and APS kinase (dark orange). The grey surfaces corresponds to the opposing monomer. *ScATPS* organizes as homohexamer. **b**, Monomers of *MtATPS* (yellow), *TtATPS* (grey), *ScATPS* (navy blue), *RrsATPS* (magenta), *GmATPS* (green) and *AaATPS* (cyan) are superposed on domain II and shown as cartoons. Abbreviations and rmsd can be found in Supplementary Table 1. **c, d**, Surface area involved in the oligomerization of *MtATPS* (**c**) and *TtATPS* (**d**). One monomer is shown in surface representation and one monomer is displayed in cartoon. The monomer-monomer contacts,

established by the domain III of one chain (in orange for *MtATPS* and black for *TtATPS*), are shown as a red surface. The wheat coloured surface highlights domain III. The framed inlet is a close up of the Zn binding motif and residues coordinating the Zn are drawn as sticks. Carbon, nitrogen and sulfur are coloured as orange/white, blue and yellow, respectively. **e, f**, Catalytic site of *MtATPS* (apo, **e**) and *TtATPS* with bound APS (**f**). Elements are coloured as in insets (**c, d**) with oxygen and phosphorus in red and orange, respectively. Residues belonging to the canonical motifs of the ATPase are highlighted by pink coloured carbon atoms.



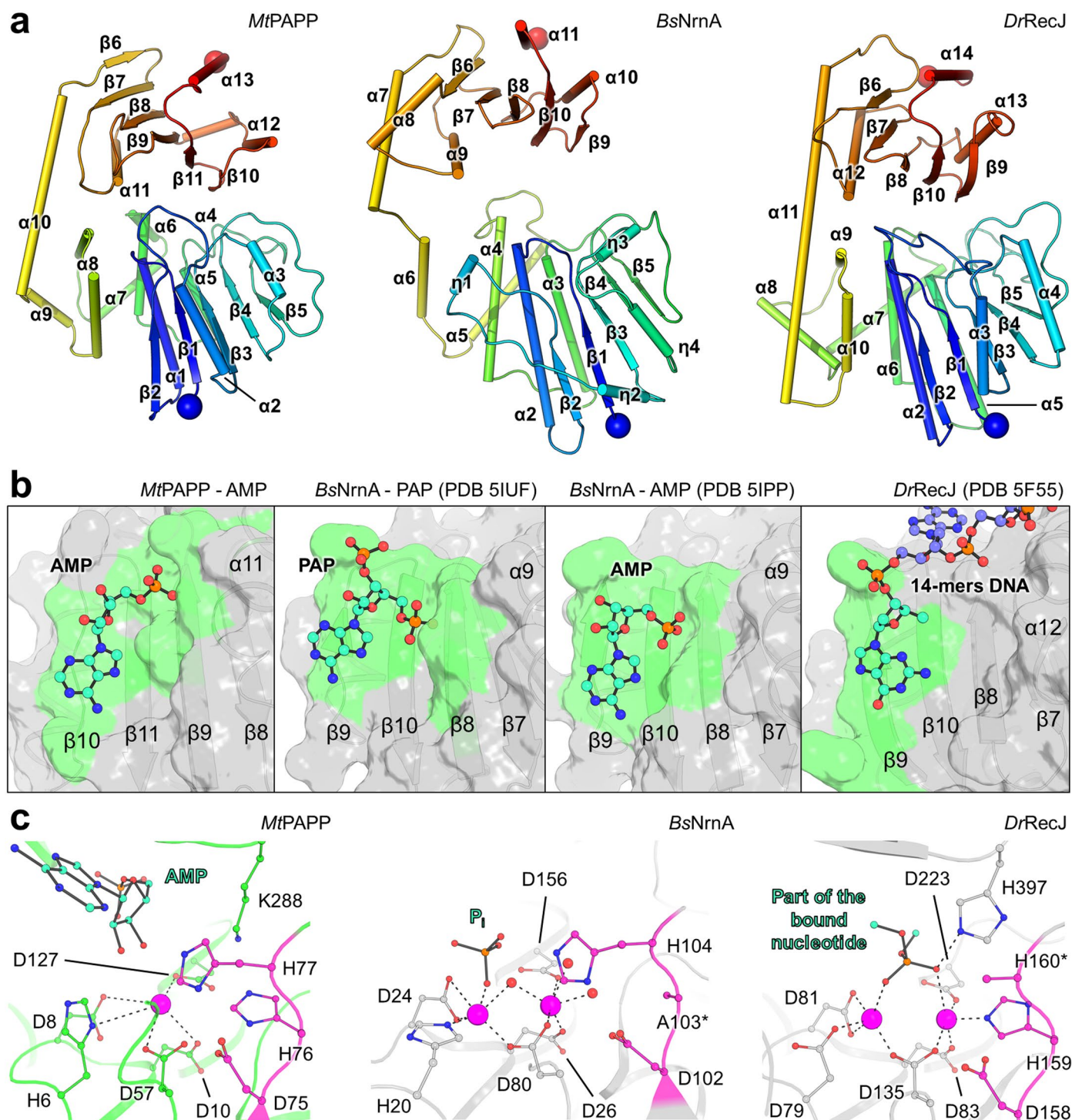
Extended Data Fig. 4 | Phylogenetic analysis of *MtATPS* and *MtAPSK*. **a**, The heterodimeric sulfate adenyltransferase (CysDN) with the homo-oligomeric ATP-dependent sulfurylase (sat) and **b**, APS-kinases. For panel a: the heterodimeric assimilatory ATP-sulfurylase is composed of a regulatory GTPase

subunit CysN (light red) and a catalytic subunit CysD (blue). Sat is involved in both assimilatory and dissimilatory SO_4^{2-} reduction (light orange). *MtATPS* and *MtAPSK* are highlighted in bold red. Bootstrap support values $\geq 90\%$ are shown as dots on interior nodes.



Extended Data Fig. 5 | *MtAPSK* belongs to the APSK family. **a**, Left panel, homodimeric *MtAPSK* apo (orange) superposed to its closest homologue *Synechocystis* sp. PCC 6803 (*SsAPSK*, white, PDB: **5CB6**) in complex with APS and AMP-PnP. The ligands are shown in sticks and spheres and the missing part 125–152 in *MtAPSK* (indicated by balls) is highlighted in black in *SsAPSK*. Carbon, nitrogen, oxygen, sulfur and phosphorus are coloured in light orange/white/cyan, blue, red, yellow and orange, respectively. Right panel: superposition of

MtAPSK (wheat), *AtAPSK* (orange, PDB: **3UIE**), *ApAPSK* (slate, PDB: **2YVU**) and *PcAPSK* (white, PDB: **1M7H**) on one monomer and shown in cartoon. The active site position is indicated by a black arrow. Abbreviations and rmsd can be found in Supplementary Table 2. **b**, **c**, Catalytic site of apo *MtAPSK* (**b**) and *SsAPSK* bound to APS and AMP-PnP (**c**). Elements are coloured as in (**a**), left panel. In (**b**), arrows indicate the missing part 125–152.



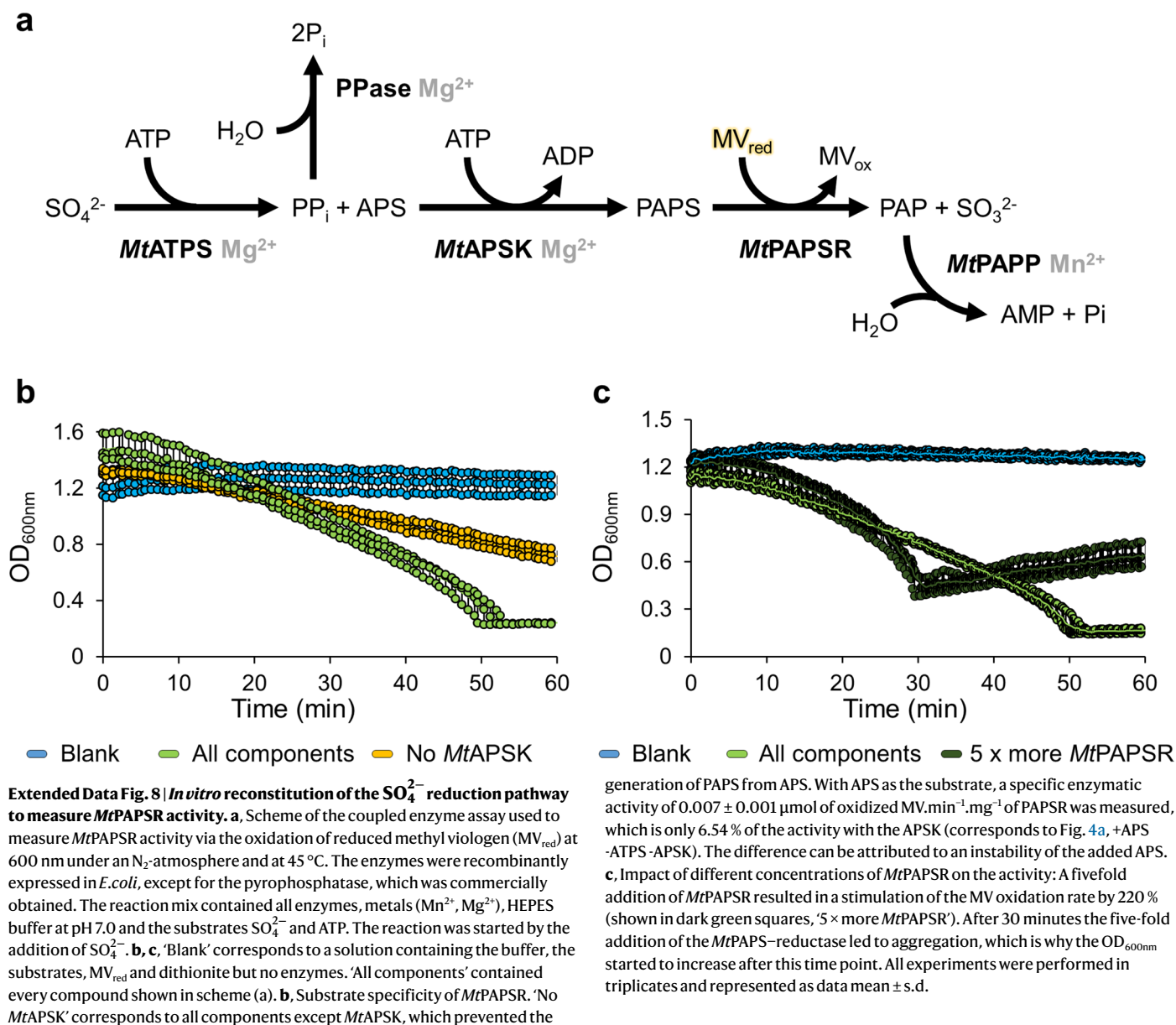
Extended Data Fig. 6 | *MtPAPP* shares similar structural features with exonucleases. a, Folding conservation across the *MtPAPP*, the NanoRNase A from *Bacillus subtilis* (*BsNrnA*, PDB: 5IUF) and the recombinase RecJ from *Deinococcus radiodurans* (*DrRecJ*, PDB: 5F55). For *BsNrnA* and *DrRecJ*, the structures only represent the DHH and DHHA1 domains and the secondary structure motifs are renumbered to simplify the comparison with *MtPAPP*. **b**, Differences in the nucleotide binding between *MtPAPP*, NanoRNase A and the recombinase RecJ with the surface residues interacting with the ligand coloured

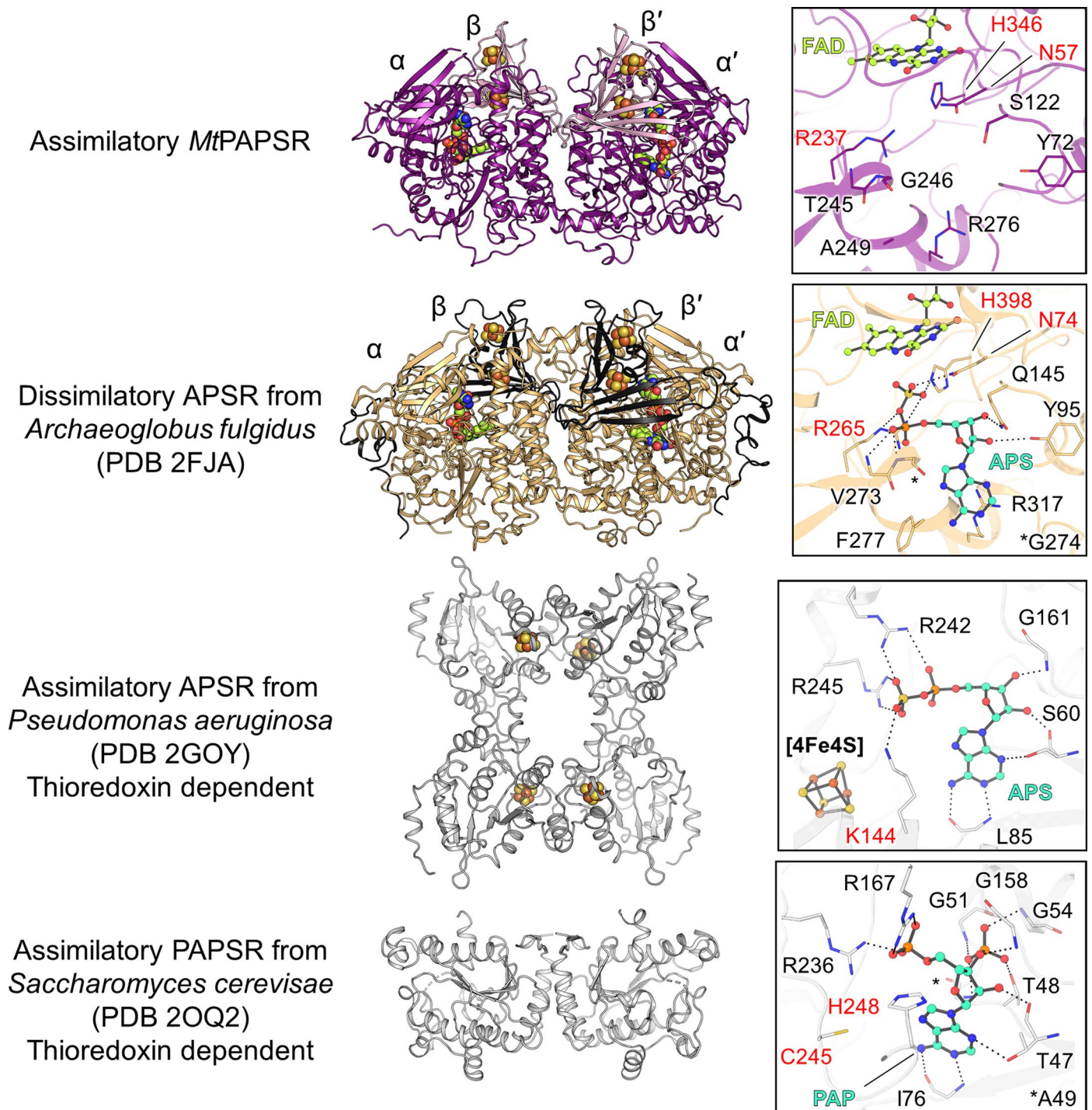
in green. **c**, Close-up of the Mn^{2+} coordination between *MtPAPP*, *BsNrnA* (PDB: 5IUF) and *DrRecJ* (PDB: 5F55). Mn^{2+} are shown as purple spheres and the residues coordinating them are highlighted as stick and balls. Carbon, nitrogen, oxygen and phosphorus atoms are coloured respectively in green/grey, blue, red and orange. Residues belonging to the canonical DHH-motif have pink coloured carbon atoms. The structure used for *BsNrnA* is the His103Ala variant, and the side chain of the His160 has not been modelled in the *DrRecJ* structure.



Extended Data Fig. 7 | Phylogenetic analysis of *MtPAPP* and *MtPAPS*.
a, PAP-phosphatases with bifunctional oligoribonucleases and PAP-phosphatases, as well as exonucleases (RecJ), and **b**, dissimilatory APS-reductases (α -subunit) and (putative) assimilatory APS/PAPS-reductases.

MtPAPS and *MtPAPP* are highlighted in bold red. Bootstrap support values $\geq 90\%$ are shown as dots on interior nodes. Asterisks (*) in front of *Methanocaldococcus jannaschii* sequences highlight the two enzymes previously biochemically characterized.





Extended Data Fig. 9 | Comparison of a dissimilatory APS-reductase and assimilatory P/APS-reductases with the *Mt*PAPSR. All structures are shown in cartoon with their (metallo)-cofactors in balls and sticks. Close-ups of the active sites (on the right) with residues important for substrate binding are highlighted as balls and sticks. The dissimilatory APS-reductase from *Archaeoglobus fulgidus* is a heterotetramer, composed of two ($\alpha\beta$)-subunits. Each β -subunit contains two [4Fe-4S]-cluster and each α -subunit one FAD. The presented assimilatory APSR

from *Pseudomonas aeruginosa* is a homotetramer. It contains one [4Fe-4S]-cluster per monomer. The assimilatory PAPSR from *Saccharomyces cerevisiae* is homodimeric. The elements oxygen, nitrogen, phosphorus, sulfur and iron are coloured red, blue, orange, yellow and brown, respectively. The carbon of the substrate/product is coloured in cyan, and in yellow for the FAD. Catalytic residues are highlighted with red labels.

Extended Data Table 1 | X-ray analysis statistics for the presented structures

	<i>Mt</i> ATPS form 1	<i>Mt</i> ATPS form 2	<i>Mt</i> APSK	<i>Mt</i> PAPP	<i>Mt</i> PAPSR Fe K edge	<i>Mt</i> PAPSR
Data collection						
Synchrotron source	SOLEIL, Proxima-I	SOLEIL Proxima-I	SLS, X06DA	SLS, X06DA	PETRAIII, P11	SLS, X06DA
Wavelength (Å)	1.00000	1.03320	1.00003	1.64566	1.73646	0.97625
Space group	<i>I</i> 222	<i>C</i> 2	<i>P</i> 2 ₁	<i>I</i> 4	<i>P</i> 2 ₁	<i>P</i> 2 ₁
Resolution (Å)	78.79 – 1.97 (2.22 – 1.97)	65.94–2.10 (2.16–2.10)	47.74– 1.77 (1.81– 1.77)	126.38 – 3.10 (3.27 – 3.10)	85.51 – 1.89 (2.17 – 1.89)	86.04 – 1.45 (1.64 – 1.45)
Cell dimensions						
a, b, c (Å)	55.70, 154.46, 157.57	185.28, 54.52, 85.43	51.54, 176.18, 51.61	174.05, 174.05, 183.80	63.53, 122.82, 88.53	63.71, 123.65, 88.84
α, β, γ (°)	90, 90, 90	90, 95.91, 90	90, 105.78, 90	90, 90, 90	90, 105.01, 90	90, 104.44, 90
R _{merge} (%) ^a	15.1 (174.0)	13.5 (114.9)	4.4 (92.8)	19.7 (248.3)	20.0 (169.8)	7.9 (105.6)
R _{pim} (%) ^a	4.2 (48.3)	5.5 (47.5)	1.8 (39.8)	5.6 (68.0)	6.9 (62.5)	3.3 (42.5)
CC _{1/2} ^a	0.998 (0.641)	0.997 (0.57)	1.0 (0.685)	0.998 (0.477)	0.998 (0.6)	0.997 (0.567)
I/σ _I ^a	12.7 (1.6)	10.2 (1.6)	22.7 (1.7)	12.3 (1.1)	12.0 (1.8)	11.9 (1.7)
Spherical completeness ^a	58.2 (9.9)	82.3 (51.2)	80.0 (64.5)	92.1 (100.0)	55.7 (8.3)	62.3 (10.2)
Ellipsoidal completeness ^a	93.2 (62.3)	95.6 (98.3)	83.1 (96.3)	/	91.8 (59.4)	95.0 (73.8)
Redundancy ^a	13.7 (13.9)	6.9 (6.6)	6.8 (6.2)	13.3 (14.3)	18.2 (14.4)	6.8 (7.1)
Nr. unique reflections ^a	28,197 (1,410)	41,069 (2,053)	68,557 (3,427)	45,681 (7,240)	58,277 (2,915)	146,296 (7,316)
Refinement						
Resolution (Å)	49.73 – 1.97	52.28 – 2.10	44.04 – 1.77	57.79 – 3.10		1.45
Number of reflections	28,185	41,057	68,551	45,643		14,6283
R _{work} /R _{free} ^b (%)	18.85/21.79	19.86/23.94	15.40/18.09	18.57/21.96		15.14/17.80
Number of atoms						
Protein	3,155	6,205	4,753	15,234		10368
Ligands/ions	49	71	88	183		223
Solvent	208	354	606	0		879
Mean B-value (Å ²)	42.81	39.09	37.12	94.96		32.18
Molprobit clash score, all atoms	2.99	2.09	3.38	4.67		3.34
Ramachandran plot						
Favoured regions (%)	97.11	97.45	99.30	96.92		97.75
Outlier regions (%)	0	0	0	0		0
rmsd ^c bond lengths (Å)	0.011	0.005	0.007	0.004		0.007
rmsd ^c bond angles (°)	1.138	0.823	0.935	0.613		0.917
PDB ID code	8A8G	8A8D	8A8H	8A8K		8A8O

^aValues relative to the highest resolution shell are within parentheses. ^bR_{free} was calculated as the R_{work} for 5% of the reflections that were not included in the refinement. ^crmsd, root mean square deviation.

Reporting Summary

Nature Portfolio wishes to improve the reproducibility of the work that we publish. This form provides structure for consistency and transparency in reporting. For further information on Nature Portfolio policies, see our [Editorial Policies](#) and the [Editorial Policy Checklist](#).

Statistics

For all statistical analyses, confirm that the following items are present in the figure legend, table legend, main text, or Methods section.

- | n/a | Confirmed |
|-------------------------------------|--|
| <input type="checkbox"/> | <input checked="" type="checkbox"/> The exact sample size (n) for each experimental group/condition, given as a discrete number and unit of measurement |
| <input type="checkbox"/> | <input checked="" type="checkbox"/> A statement on whether measurements were taken from distinct samples or whether the same sample was measured repeatedly |
| <input checked="" type="checkbox"/> | <input type="checkbox"/> The statistical test(s) used AND whether they are one- or two-sided
<i>Only common tests should be described solely by name; describe more complex techniques in the Methods section.</i> |
| <input checked="" type="checkbox"/> | <input type="checkbox"/> A description of all covariates tested |
| <input checked="" type="checkbox"/> | <input type="checkbox"/> A description of any assumptions or corrections, such as tests of normality and adjustment for multiple comparisons |
| <input type="checkbox"/> | <input checked="" type="checkbox"/> A full description of the statistical parameters including central tendency (e.g. means) or other basic estimates (e.g. regression coefficient) AND variation (e.g. standard deviation) or associated estimates of uncertainty (e.g. confidence intervals) |
| <input checked="" type="checkbox"/> | <input type="checkbox"/> For null hypothesis testing, the test statistic (e.g. F , t , r) with confidence intervals, effect sizes, degrees of freedom and P value noted
<i>Give P values as exact values whenever suitable.</i> |
| <input checked="" type="checkbox"/> | <input type="checkbox"/> For Bayesian analysis, information on the choice of priors and Markov chain Monte Carlo settings |
| <input checked="" type="checkbox"/> | <input type="checkbox"/> For hierarchical and complex designs, identification of the appropriate level for tests and full reporting of outcomes |
| <input checked="" type="checkbox"/> | <input type="checkbox"/> Estimates of effect sizes (e.g. Cohen's d , Pearson's r), indicating how they were calculated |

Our web collection on [statistics for biologists](#) contains articles on many of the points above.

Software and code

Policy information about [availability of computer code](#)

Data collection Spectrophotometer for growth measurement: Spectrophotometer UV/VIS UVmini-1240 SHIMADZU.
Ion-Chromatography: Metrohm 930 Compact IC Flex.
Plate reader: SPECTROstar® Nano Microplate Reader and Omega multi-mode Microplate Reader.
Synchrotron data collection are all stated in the Extended Data Table.

Data analysis Microsoft Excel 16 (16.05356.1000)
IC MagIC Net 3.2
MEGA version 11.0
autoPROC 1.0.5 (20201211)
XDS (for MtPAPP), VERSION Feb 5, 2021 BUILT=20210323
SCALA (for MtPAPP) version 3.3.22 from CCP4 package 7.0.078
PHENIX 1.19.2_4158
CRANK2, version 2.0.227
COOT version 0.8.9.2
Open-source Pymol Version 2.2.0

For manuscripts utilizing custom algorithms or software that are central to the research but not yet described in published literature, software must be made available to editors and reviewers. We strongly encourage code deposition in a community repository (e.g. GitHub). See the Nature Portfolio [guidelines for submitting code & software](#) for further information.

Data

Policy information about [availability of data](#)

All manuscripts must include a [data availability statement](#). This statement should provide the following information, where applicable:

- Accession codes, unique identifiers, or web links for publicly available datasets
- A description of any restrictions on data availability
- For clinical datasets or third party data, please ensure that the statement adheres to our [policy](#)

All structures used for structural comparison are accessible on the Protein Data Bank and accordingly cited in the text. The structures were deposited in the protein data bank under the ID: 8A8G for MtATPS form 1, 8A8D for MtATPS form 2, 8A8H for MtAPSK, 8A8K for MtPAPP and 8A8O for MtPAPSR. The data for this study are available in the paper and in the Supplementary Information. Source data are provided with this paper.

Human research participants

Policy information about [studies involving human research participants and Sex and Gender in Research](#).

Reporting on sex and gender

n.a.

Population characteristics

n.a.

Recruitment

n.a.

Ethics oversight

n.a.

Note that full information on the approval of the study protocol must also be provided in the manuscript.

Field-specific reporting

Please select the one below that is the best fit for your research. If you are not sure, read the appropriate sections before making your selection.

Life sciences Behavioural & social sciences Ecological, evolutionary & environmental sciences

For a reference copy of the document with all sections, see [nature.com/documents/nr-reporting-summary-flat.pdf](https://www.nature.com/documents/nr-reporting-summary-flat.pdf)

Life sciences study design

All studies must disclose on these points even when the disclosure is negative.

Sample size

Three biological replicates were performed for the growth experiments, except if stated otherwise. Sample sizes were chosen based on statistical relevancy. Error bars were omitted for duplicates.
The ion-chromatography measurements were also performed in biological triplicates. For all enzymatic assays, experimental triplicates were performed.

Data exclusions

No data was excluded from the analyses

Replication

All replicates were successful. The number of replicates are mentioned in the text.

Randomization

Randomization were applied to generate the Rfree set for the protein refinement. Except for structural analyses, randomization was not applied.

Blinding

N/A. Each biological and biochemical experiment in this study is rationally designed and leads to a specific conclusion, therefore, blinding was not required in this study.

Behavioural & social sciences study design

All studies must disclose on these points even when the disclosure is negative.

Study description

Briefly describe the study type including whether data are quantitative, qualitative, or mixed-methods (e.g. qualitative cross-sectional, quantitative experimental, mixed-methods case study).

Research sample

State the research sample (e.g. Harvard university undergraduates, villagers in rural India) and provide relevant demographic

Research sample	<i>information (e.g. age, sex) and indicate whether the sample is representative. Provide a rationale for the study sample chosen. For studies involving existing datasets, please describe the dataset and source.</i>
Sampling strategy	<i>Describe the sampling procedure (e.g. random, snowball, stratified, convenience). Describe the statistical methods that were used to predetermine sample size OR if no sample-size calculation was performed, describe how sample sizes were chosen and provide a rationale for why these sample sizes are sufficient. For qualitative data, please indicate whether data saturation was considered, and what criteria were used to decide that no further sampling was needed.</i>
Data collection	<i>Provide details about the data collection procedure, including the instruments or devices used to record the data (e.g. pen and paper, computer, eye tracker, video or audio equipment) whether anyone was present besides the participant(s) and the researcher, and whether the researcher was blind to experimental condition and/or the study hypothesis during data collection.</i>
Timing	<i>Indicate the start and stop dates of data collection. If there is a gap between collection periods, state the dates for each sample cohort.</i>
Data exclusions	<i>If no data were excluded from the analyses, state so OR if data were excluded, provide the exact number of exclusions and the rationale behind them, indicating whether exclusion criteria were pre-established.</i>
Non-participation	<i>State how many participants dropped out/declined participation and the reason(s) given OR provide response rate OR state that no participants dropped out/declined participation.</i>
Randomization	<i>If participants were not allocated into experimental groups, state so OR describe how participants were allocated to groups, and if allocation was not random, describe how covariates were controlled.</i>

Ecological, evolutionary & environmental sciences study design

All studies must disclose on these points even when the disclosure is negative.

Study description	<i>Briefly describe the study. For quantitative data include treatment factors and interactions, design structure (e.g. factorial, nested, hierarchical), nature and number of experimental units and replicates.</i>
Research sample	<i>Describe the research sample (e.g. a group of tagged <i>Passer domesticus</i>, all <i>Stenocereus thurberi</i> within Organ Pipe Cactus National Monument), and provide a rationale for the sample choice. When relevant, describe the organism taxa, source, sex, age range and any manipulations. State what population the sample is meant to represent when applicable. For studies involving existing datasets, describe the data and its source.</i>
Sampling strategy	<i>Note the sampling procedure. Describe the statistical methods that were used to predetermine sample size OR if no sample-size calculation was performed, describe how sample sizes were chosen and provide a rationale for why these sample sizes are sufficient.</i>
Data collection	<i>Describe the data collection procedure, including who recorded the data and how.</i>
Timing and spatial scale	<i>Indicate the start and stop dates of data collection, noting the frequency and periodicity of sampling and providing a rationale for these choices. If there is a gap between collection periods, state the dates for each sample cohort. Specify the spatial scale from which the data are taken</i>
Data exclusions	<i>If no data were excluded from the analyses, state so OR if data were excluded, describe the exclusions and the rationale behind them, indicating whether exclusion criteria were pre-established.</i>
Reproducibility	<i>Describe the measures taken to verify the reproducibility of experimental findings. For each experiment, note whether any attempts to repeat the experiment failed OR state that all attempts to repeat the experiment were successful.</i>
Randomization	<i>Describe how samples/organisms/participants were allocated into groups. If allocation was not random, describe how covariates were controlled. If this is not relevant to your study, explain why.</i>
Blinding	<i>Describe the extent of blinding used during data acquisition and analysis. If blinding was not possible, describe why OR explain why blinding was not relevant to your study.</i>

Did the study involve field work? Yes No

Field work, collection and transport

Field conditions	<i>Describe the study conditions for field work, providing relevant parameters (e.g. temperature, rainfall).</i>
Location	<i>State the location of the sampling or experiment, providing relevant parameters (e.g. latitude and longitude, elevation, water depth).</i>
Access & import/export	<i>Describe the efforts you have made to access habitats and to collect and import/export your samples in a responsible manner and in</i>

Access & import/export *compliance with local, national and international laws, noting any permits that were obtained (give the name of the issuing authority, the date of issue, and any identifying information).*

Disturbance *Describe any disturbance caused by the study and how it was minimized.*

Reporting for specific materials, systems and methods

We require information from authors about some types of materials, experimental systems and methods used in many studies. Here, indicate whether each material, system or method listed is relevant to your study. If you are not sure if a list item applies to your research, read the appropriate section before selecting a response.

Materials & experimental systems

- | | |
|-------------------------------------|--|
| n/a | Involved in the study |
| <input checked="" type="checkbox"/> | <input type="checkbox"/> Antibodies |
| <input checked="" type="checkbox"/> | <input type="checkbox"/> Eukaryotic cell lines |
| <input checked="" type="checkbox"/> | <input type="checkbox"/> Palaeontology and archaeology |
| <input checked="" type="checkbox"/> | <input type="checkbox"/> Animals and other organisms |
| <input checked="" type="checkbox"/> | <input type="checkbox"/> Clinical data |
| <input checked="" type="checkbox"/> | <input type="checkbox"/> Dual use research of concern |

Methods

- | | |
|-------------------------------------|---|
| n/a | Involved in the study |
| <input checked="" type="checkbox"/> | <input type="checkbox"/> ChIP-seq |
| <input checked="" type="checkbox"/> | <input type="checkbox"/> Flow cytometry |
| <input checked="" type="checkbox"/> | <input type="checkbox"/> MRI-based neuroimaging |

Antibodies

Antibodies used *Describe all antibodies used in the study; as applicable, provide supplier name, catalog number, clone name, and lot number.*

Validation *Describe the validation of each primary antibody for the species and application, noting any validation statements on the manufacturer's website, relevant citations, antibody profiles in online databases, or data provided in the manuscript.*

Eukaryotic cell lines

Policy information about [cell lines and Sex and Gender in Research](#)

Cell line source(s) *State the source of each cell line used and the sex of all primary cell lines and cells derived from human participants or vertebrate models.*

Authentication *Describe the authentication procedures for each cell line used OR declare that none of the cell lines used were authenticated.*

Mycoplasma contamination *Confirm that all cell lines tested negative for mycoplasma contamination OR describe the results of the testing for mycoplasma contamination OR declare that the cell lines were not tested for mycoplasma contamination.*

Commonly misidentified lines (See [ICLAC](#) register) *Name any commonly misidentified cell lines used in the study and provide a rationale for their use.*

Palaeontology and Archaeology

Specimen provenance *Provide provenance information for specimens and describe permits that were obtained for the work (including the name of the issuing authority, the date of issue, and any identifying information). Permits should encompass collection and, where applicable, export.*

Specimen deposition *Indicate where the specimens have been deposited to permit free access by other researchers.*

Dating methods *If new dates are provided, describe how they were obtained (e.g. collection, storage, sample pretreatment and measurement), where they were obtained (i.e. lab name), the calibration program and the protocol for quality assurance OR state that no new dates are provided.*

Tick this box to confirm that the raw and calibrated dates are available in the paper or in Supplementary Information.

Ethics oversight *Identify the organization(s) that approved or provided guidance on the study protocol, OR state that no ethical approval or guidance was required and explain why not.*

Note that full information on the approval of the study protocol must also be provided in the manuscript.

Animals and other research organisms

Policy information about [studies involving animals](#); [ARRIVE guidelines](#) recommended for reporting animal research, and [Sex and Gender in Research](#)

Laboratory animals	<i>For laboratory animals, report species, strain and age OR state that the study did not involve laboratory animals.</i>
Wild animals	<i>Provide details on animals observed in or captured in the field; report species and age where possible. Describe how animals were caught and transported and what happened to captive animals after the study (if killed, explain why and describe method; if released, say where and when) OR state that the study did not involve wild animals.</i>
Reporting on sex	<i>Indicate if findings apply to only one sex; describe whether sex was considered in study design, methods used for assigning sex. Provide data disaggregated for sex where this information has been collected in the source data as appropriate; provide overall numbers in this Reporting Summary. Please state if this information has not been collected. Report sex-based analyses where performed, justify reasons for lack of sex-based analysis.</i>
Field-collected samples	<i>For laboratory work with field-collected samples, describe all relevant parameters such as housing, maintenance, temperature, photoperiod and end-of-experiment protocol OR state that the study did not involve samples collected from the field.</i>
Ethics oversight	<i>Identify the organization(s) that approved or provided guidance on the study protocol, OR state that no ethical approval or guidance was required and explain why not.</i>

Note that full information on the approval of the study protocol must also be provided in the manuscript.

Clinical data

Policy information about [clinical studies](#)

All manuscripts should comply with the ICMJE [guidelines for publication of clinical research](#) and a completed [CONSORT checklist](#) must be included with all submissions.

Clinical trial registration	<i>Provide the trial registration number from ClinicalTrials.gov or an equivalent agency.</i>
Study protocol	<i>Note where the full trial protocol can be accessed OR if not available, explain why.</i>
Data collection	<i>Describe the settings and locales of data collection, noting the time periods of recruitment and data collection.</i>
Outcomes	<i>Describe how you pre-defined primary and secondary outcome measures and how you assessed these measures.</i>

Dual use research of concern

Policy information about [dual use research of concern](#)

Hazards

Could the accidental, deliberate or reckless misuse of agents or technologies generated in the work, or the application of information presented in the manuscript, pose a threat to:

No	Yes	
<input type="checkbox"/>	<input type="checkbox"/>	Public health
<input type="checkbox"/>	<input type="checkbox"/>	National security
<input type="checkbox"/>	<input type="checkbox"/>	Crops and/or livestock
<input type="checkbox"/>	<input type="checkbox"/>	Ecosystems
<input type="checkbox"/>	<input type="checkbox"/>	Any other significant area

Experiments of concern

Does the work involve any of these experiments of concern:

- | No | Yes | |
|--------------------------|--------------------------|---|
| <input type="checkbox"/> | <input type="checkbox"/> | Demonstrate how to render a vaccine ineffective |
| <input type="checkbox"/> | <input type="checkbox"/> | Confer resistance to therapeutically useful antibiotics or antiviral agents |
| <input type="checkbox"/> | <input type="checkbox"/> | Enhance the virulence of a pathogen or render a nonpathogen virulent |
| <input type="checkbox"/> | <input type="checkbox"/> | Increase transmissibility of a pathogen |
| <input type="checkbox"/> | <input type="checkbox"/> | Alter the host range of a pathogen |
| <input type="checkbox"/> | <input type="checkbox"/> | Enable evasion of diagnostic/detection modalities |
| <input type="checkbox"/> | <input type="checkbox"/> | Enable the weaponization of a biological agent or toxin |
| <input type="checkbox"/> | <input type="checkbox"/> | Any other potentially harmful combination of experiments and agents |

ChIP-seq

Data deposition

- Confirm that both raw and final processed data have been deposited in a public database such as [GEO](#).
- Confirm that you have deposited or provided access to graph files (e.g. BED files) for the called peaks.

Data access links

May remain private before publication.

For "Initial submission" or "Revised version" documents, provide reviewer access links. For your "Final submission" document, provide a link to the deposited data.

Files in database submission

Provide a list of all files available in the database submission.

Genome browser session

(e.g. [UCSC](#))

Provide a link to an anonymized genome browser session for "Initial submission" and "Revised version" documents only, to enable peer review. Write "no longer applicable" for "Final submission" documents.

Methodology

Replicates

Describe the experimental replicates, specifying number, type and replicate agreement.

Sequencing depth

Describe the sequencing depth for each experiment, providing the total number of reads, uniquely mapped reads, length of reads and whether they were paired- or single-end.

Antibodies

Describe the antibodies used for the ChIP-seq experiments; as applicable, provide supplier name, catalog number, clone name, and lot number.

Peak calling parameters

Specify the command line program and parameters used for read mapping and peak calling, including the ChIP, control and index files used.

Data quality

Describe the methods used to ensure data quality in full detail, including how many peaks are at FDR 5% and above 5-fold enrichment.

Software

Describe the software used to collect and analyze the ChIP-seq data. For custom code that has been deposited into a community repository, provide accession details.

Flow Cytometry

Plots

Confirm that:

- The axis labels state the marker and fluorochrome used (e.g. CD4-FITC).
- The axis scales are clearly visible. Include numbers along axes only for bottom left plot of group (a 'group' is an analysis of identical markers).
- All plots are contour plots with outliers or pseudocolor plots.
- A numerical value for number of cells or percentage (with statistics) is provided.

Methodology

Sample preparation

Describe the sample preparation, detailing the biological source of the cells and any tissue processing steps used.

Instrument

Identify the instrument used for data collection, specifying make and model number.

Software *Describe the software used to collect and analyze the flow cytometry data. For custom code that has been deposited into a community repository, provide accession details.*

Cell population abundance *Describe the abundance of the relevant cell populations within post-sort fractions, providing details on the purity of the samples and how it was determined.*

Gating strategy *Describe the gating strategy used for all relevant experiments, specifying the preliminary FSC/SSC gates of the starting cell population, indicating where boundaries between "positive" and "negative" staining cell populations are defined.*

Tick this box to confirm that a figure exemplifying the gating strategy is provided in the Supplementary Information.

Magnetic resonance imaging

Experimental design

Design type *Indicate task or resting state; event-related or block design.*

Design specifications *Specify the number of blocks, trials or experimental units per session and/or subject, and specify the length of each trial or block (if trials are blocked) and interval between trials.*

Behavioral performance measures *State number and/or type of variables recorded (e.g. correct button press, response time) and what statistics were used to establish that the subjects were performing the task as expected (e.g. mean, range, and/or standard deviation across subjects).*

Acquisition

Imaging type(s) *Specify: functional, structural, diffusion, perfusion.*

Field strength *Specify in Tesla*

Sequence & imaging parameters *Specify the pulse sequence type (gradient echo, spin echo, etc.), imaging type (EPI, spiral, etc.), field of view, matrix size, slice thickness, orientation and TE/TR/flip angle.*

Area of acquisition *State whether a whole brain scan was used OR define the area of acquisition, describing how the region was determined.*

Diffusion MRI Used Not used

Preprocessing

Preprocessing software *Provide detail on software version and revision number and on specific parameters (model/functions, brain extraction, segmentation, smoothing kernel size, etc.).*

Normalization *If data were normalized/standardized, describe the approach(es): specify linear or non-linear and define image types used for transformation OR indicate that data were not normalized and explain rationale for lack of normalization.*

Normalization template *Describe the template used for normalization/transformation, specifying subject space or group standardized space (e.g. original Talairach, MNI305, ICBM152) OR indicate that the data were not normalized.*

Noise and artifact removal *Describe your procedure(s) for artifact and structured noise removal, specifying motion parameters, tissue signals and physiological signals (heart rate, respiration).*

Volume censoring *Define your software and/or method and criteria for volume censoring, and state the extent of such censoring.*

Statistical modeling & inference

Model type and settings *Specify type (mass univariate, multivariate, RSA, predictive, etc.) and describe essential details of the model at the first and second levels (e.g. fixed, random or mixed effects; drift or auto-correlation).*

Effect(s) tested *Define precise effect in terms of the task or stimulus conditions instead of psychological concepts and indicate whether ANOVA or factorial designs were used.*

Specify type of analysis: Whole brain ROI-based Both

Statistic type for inference (See [Eklund et al. 2016](#)) *Specify voxel-wise or cluster-wise and report all relevant parameters for cluster-wise methods.*

Correction *Describe the type of correction and how it is obtained for multiple comparisons (e.g. FWE, FDR, permutation or Monte Carlo).*

Models & analysis

- n/a | Involved in the study
- Functional and/or effective connectivity
- Graph analysis
- Multivariate modeling or predictive analysis

Functional and/or effective connectivity

Report the measures of dependence used and the model details (e.g. Pearson correlation, partial correlation, mutual information).

Graph analysis

Report the dependent variable and connectivity measure, specifying weighted graph or binarized graph, subject- or group-level, and the global and/or node summaries used (e.g. clustering coefficient, efficiency, etc.).

Multivariate modeling and predictive analysis

Specify independent variables, features extraction and dimension reduction, model, training and evaluation metrics.